THESIS

BARIUM SENSING IN HOLLOW CATHODE PLASMA USING CAVITY RING-DOWN SPECTROSCOPY (CRDS)

Submitted by

Seth Antozzi

Department of Mechanical Engineering

In partial fulfillment of the requirements

For the Degree of Master of Science

Colorado State University

Fort Collins, Colorado

Fall 2024

Master's Committee:

Advisor: Azer Yalin

Ciprian Dumitrache
David Aristoff

ABSTRACT

BARIUM SENSING IN HOLLOW CATHODE PLASMA USING CAVITY RING-DOWN SPECTROSCOPY (CRDS)

Hollow cathodes (HCs) are ion propulsion devices commonly paired with Hall Effect Thrusters (HETs), which are devices of increasing importance in the ion propulsion community. Barium Oxide (BaO) cathodes are known to emit barium when operating under high-temperature conditions. Understanding barium densities in the cathode plasma provides experimental guidance for NASA barium modeling, including understanding of the physical characteristics and lifetime of the cathode. Based on modeling work, expected barium densities are ~10^{10} cm^{-3}. A sensitive diagnostic is required such as CRDS. In this work, the detection of barium from the thermionic emitter of the Mark II 25 A BaO HC using the laser diagnostic technique of cavity ring-down spectroscopy (CRDS) is presented. CRDS detects ground state neutral barium via absorption of the probe laser beam in the vicinity of 553.548 nm (air wavelength). The cathode CRDS measurements are performed along the axis of the cathode since that is the control volume of interest. We report barium density as a function of heater current (plasma off) with results showing an approximately exponential density increase with current. Further parameters of study include keeper current, anode current (with the cathode operating), and propellant flow values. The measured signal-to-noise allows estimation of the barium density detection limit as ~10^{6} cm^{-3} in the present configuration.

An appendix to this work addresses the need for a diagnostic technique to measure krypton neutrals in HC plumes. In the krypton study, we enhance the krypton Two-Photon Absorption

Laser Induced Fluorescence (TALIF) technique and apply it to a BaO HC plasma. We utilize a dye laser at 212.6 nm to excite TALIF fluorescence within the plume, with the fluorescence detected at 758.7 nm. We present spatial maps for krypton neutral densities at a cathode flow rate of 7.5 sccm and anode currents of 5A and 13A. These measurements provide insights into facility effects related to cathode coupling and cathode physics, such as the collisional damping of instabilities. Additionally, we discuss how plasma characteristics, including spot versus plume mode, and plasma luminosity, are influenced.

ACKNOWLEDGEMENTS

All research for my thesis has been supported by NASA through the Joint Advanced Propulsion Institute, a NASA Space Technology Research Institute, grant number 80NSSC21K1118.

DEDICATION

A very warm thank you to all who have walked this crazy graduate school journey with me! For technical help with the HCs, the assistance and knowledge (and timely spot welding) of the cathode-whisperer Professor John Williams, Seth Thompson, and Emily Ku was truly valuable, thanks a million. The help of my teammates such as the illustrious Jacob Gottfried (we miss you), Parneeth Lokini (good at cricket and lasers), Evan Ronzone (electrical whiz and oil wrangler), and Seth Wilson (LabVIEW genius who wears cool boots) was critical. Spencer Teeter, Katie Plese, and Mohzdeh Hooshyar, always nice to talk aerospace with you all when I was taking a break from data collection, you kept me going. To Jon Stienike (why am I getting no signal?), Neylson Rodrigues (FRCC was a long time ago!), and Brian Harrod (thanks for helping with turbopump cooling systems), it was great working alongside you, and I know you will put out amazing papers. A sincere thank you to my advisor Professor Azer Yalin, especially for the advice at moments of stress! And Dr. Ciprian Dumitrache, thanks for the encouraging comments about how to be a better researcher.

Finally, on a very personal level, my Antozzi family (Dad, Mom, Sarah [Sarah, grammar suggestions were appreciated!], I truly could not have done this without you and your timely interventions for a trip to Krazy Karl's when I was about to become Krazy Seth). Shout out to my circle of friends, good times with group dinners and making "grouches" (don't ask) got me through. And ultimately, to the One I do everything for, thank You Jesus for being God, my Savior, and my Friend.

TABLE OF CONTENTS

LIST OF FIGURES

Chapter 1- Introduction

1.1 Introduction to Ion Propulsion

Ion propulsion (also known as electric propulsion) is a growing field of study in the aerospace industry. Research involving ion propulsion dates to the early 1900s, but the first experimental ion thruster prototypes were not flown until the 1960s by both the USA and Russian space programs [1]. Beginning in the 1970s, significant use of ion thrusters began, including use cases such as thrusters used for satellite station-keeping [1]. Although station-keeping is a common use case for ion propulsion, interest has also grown in ion propulsion as a deep-space mission propulsion method that offers high efficiency and high Δv. The Δv factors are stated in equation (1), in which *Isp* is specific impulse, g gravity, m_d delivered mass, and m_p propellant mass). Note that for an ion propulsion device, *Isp* is quite large, as high as 7000 s, which is a function of the higher exit velocities that are also characteristic of the device [1]. Use cases include such recent missions as NASA's DAWN and DART [2,3].

$$\Delta v = (\mathrm{Isp} * \mathrm{g}) \ln\left(\frac{m_d + m_p}{m_d}\right) \quad (1)$$

A leading ion thruster type for such missions is the Hall Effect Thruster (HET), which was utilized on recent missions such as Psyche [4], and is a major component of the propulsion system for the Advanced Electric Propulsion System that will be used on the Artemis missions [5]. HETs are paired with HCs, with the cathodes providing the electrons necessary for the Hall effect [1]. HETs operate with less efficiency and lower specific impulse than that of some ion devices such as gridded ion thrusters, but HETs produce higher thrust per unit of power, and are overall simpler devices to operate [1].

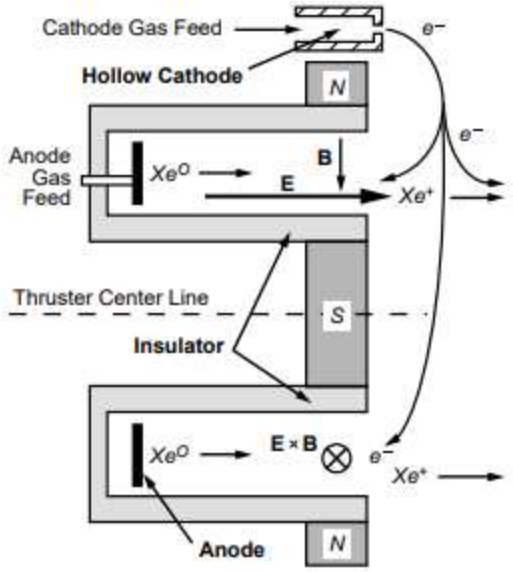

Figure 1. HET showing Hall current and cathode [1].

Features of HET operation are shown here, in Figures 1-3. A magnetic field is induced across the thruster, and gas propellant, often a noble gas such as krypton or xenon, is fed into the thruster primarily through the anode, with a small percentage through the cathode. The cathode is most often located offset from the thruster face as shown and is the electron source. The electrons are attracted to the anode's positive charge, but due to the magnetic field are slowed from reaching the anode. In this process, the electrons begin to spin around the thruster center, following the **ExB** direction and producing what is known as the Hall current. The electrons collide with the propellant atoms, and produce ions, which are accelerated away from the anode by the positive bias, providing the thrust [1].

The cathode serves two main roles, both by producing electrons. One, to produce ions as mentioned above. Two, to balance charges on the spacecraft, since otherwise a negative charge build up would occur as the thruster emits ions [1].

HCs provide the electrons from a low work-function material inside the cathode, as seen in Figure 2, where the material is the barium-impregnated emitter.

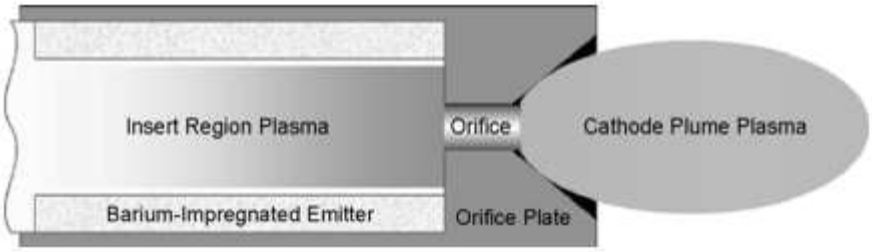

Figure 2. HC geometry, showing insert region, with low work-function material [1].

The choice of a low work-function material is important, to avoid extreme temperatures that would otherwise be necessary to release electrons. The necessary temperatures of ~2600 K seen in early designs have been improved to ~1400 K in current designs by using BaO emitters.

Typical materials for cathode emitters include cermet, lanthanum hexaboride (LaB_6), and BaO [6]. Of the three materials mentioned, BaO has the lowest work function of 2.06 eV [6]. However, of the insert materials mentioned above, BaO has the greatest risk of poisoning, due to the need for a barium dipole, which lowers the work function by reacting with tungsten, which is a substrate material present in BaO cathode emitters [6]. BaO emitters react with H_2O vapor and atmospheric gases including O_2 to form tungstates on the emitter, which shorten the life of the cathode [7]. Therefore, care must be taken to avoid poisoning the cathode via either atmospheric exposure or impurities from leaks in the gas feed system.

A typical cathode with heater and keeper is shown in Figure 3 below. Here the gas propellant feeds in from the left, enters the insert area, in which the low-work function emitter releases electrons. The newly formed plasma exits the orifice on the right to the anode downstream.

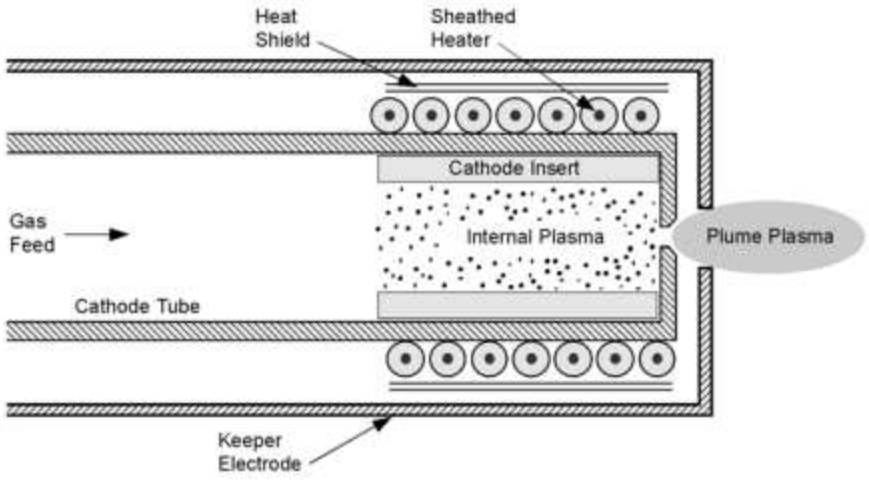

Figure 3. HC assembly, with heater, cathode, and keeper [1].

The BaO emitter releases barium as an exponential function of temperature, due to evaporation from the barium emitter, and also due to sputtering, such as that caused by ion charge-exchange reactions and plasma-heating [8]. Although BaO emitters do have contamination risks as mentioned above, they are used in many applications for ion propulsion due to their resilience against erosion. Overall, better understanding of the chemical processes that are involved with the electron emitter surface chemistry evolution and operating temperature would better inform future use cases for NASA ion propulsion applications. Particularly, it would be valuable to measure the densities of species that are emitted within the cathode plasma, in order to provide experimental results for cathode modeling. Measuring barium will provide the experimental results as mentioned above, while also potentially enabling a cathode lifetime characterization tool.

Measuring barium densities within cathode plasma is challenging because the barium population values are low, needing a very sensitive measurement capability, and also because cathodes are compact, liming access to the cathode interior. Despite these issues, some measurements have been made of neutral barium within cathodes. Crofton et. al. measured neutral

barium using a FM spectroscopic technique, as emitted by the cathode heater [9]. However, their detection limit was ~10^8 cm^{-3}, while laser diagnostic techniques can measure ~10^6 [9,10].

A technique that allows for high measurement sensitivity and access to difficult measurement volumes would solve both challenges. In the next section, CRDS as laser diagnostic for achieving these goals is introduced.

1.2 Introduction to Cavity Ring-Down Spectroscopy (CRDS)

Laser absorption spectroscopy is a laser diagnostic, which uses a laser tuned to the resonant wavelength of an absorbing medium. The laser propagates through the medium, and the light intensity is attenuated. This change in light intensity is multiplied using some form of photodetector. This intensity change can be used to calculate the density of the absorbing medium. The main limitation of this method is using only one pass of the laser light through the medium, limiting the sensitivity of the diagnostic, and hence the detection limit.

A laser diagnostic of choice in lower population density environments is Cavity Ring-Down Spectroscopy (CRDS). CRDS works by introducing two high-reflectivity (HR) mirrors into the laser beam path, to form an optical cavity. The mirrors have a high reflectivity, ~99.99% for most typical applications. The reflectivity is the limiting factor for the number of passes the beam achieves through the medium, and therefore the optical cavity length. The light that enters the optical cavity in the absence of an absorbing medium does eventually leave the cavity through leakage through the mirrors. If the optical decay, which is also termed the ring-down, is measured, the reflectivity of the mirrors may be measured. The relevant equation for this ring-down value is as given below in equation (2):

$$I_{out} = I_0 \exp\left[-\frac{t}{\tau_0}\right], \text{ where } \tau_0 = \frac{l}{(1-R)c} \tag{2}$$

where I_{out} is the decaying beam intensity exiting the cavity, l is the cavity length, I_0 is the initial beam intensity, t is time, R is cavity mirror reflectivity, c is speed of light, and τ_0 is the empty-cavity ring-down time [11].

So far the measurement of the mirror reflectivity and the meaning of the ring-down τ_0 has been considered. Once an absorbing medium is inserted, the resulting ring-down will give the absorption value. This is done by bringing the laser to a resonant wavelength for the absorber, which will give a new, lower ring-down time, τ, as follows:

$$\frac{1}{\tau(\nu)} = \frac{c}{l}[\int k(c,\nu)dx + (1-R)] \tag{3}$$

where k is the sample absorption coefficient, ν is the laser frequency [12], and the x-integration is over the length where the absorber is present. An important value is mirror loss, which can occur from both absorption and scattering, given by the term $1-R$. We can generally assume that the laser lineshape may be given as a function of frequency, $L(\nu)$, in which case we can calculate the effective absorption coefficient, k_{eff}, as follows:

$$k_{eff}(\nu) = \int_{-\infty}^{\infty} d\nu' L(\nu'-\nu)k(\nu'). \tag{4}$$

A typical approach is to tune the laser over the absorption line, allowing measurement of both τ_0 and τ, of which the difference of the reciprocals are used to calculate the dimensionless sample absorbance abs_{eff}:

$$abs_{eff}(\nu) = l_{abs}k_{eff}(\nu) = \frac{l}{c}[\frac{1}{\tau(\nu)} - \frac{1}{\tau_0}] \tag{5}$$

where l_{abs} is the length of the absorption volume. See figure 4 for an example of this ring-down difference as caused by an absorbing medium.

Considering the effect of placing an absorbing sample within the optical cavity, the ring-down time is seen to decrease, and the resulting number density of the sample can be calculated by multiplying the absorbance from equation (5) by the necessary spectral constants. The path-integrated number density of the absorber is as follows:

$$\int N_i dx = 8\pi \frac{g_i}{g_k} \frac{\nu_{ki}^2}{A_{ki} c^2} [\int abs_{eff}(\nu) d\nu] \tag{6}$$

where $\int N_i dx$ is the absorber number density integrated along the beam, g_i and g_k are degeneracies, ν_{ki} is the transition frequency, A_{ki} is the Einstein coefficient of the transition, and $\int abs_{eff}(\nu) d\nu$ is the area of the measured absorption spectrum. For our species of interest, the barium transition, the spectroscopic parameters are as follows: $g_i = 1$, $g_k = 3$, $A_{ki} = 1.19 \times 10^8\ s^{-1}$, $\nu_{ki} = 5.41 \times 10^{14}$ Hz [13].

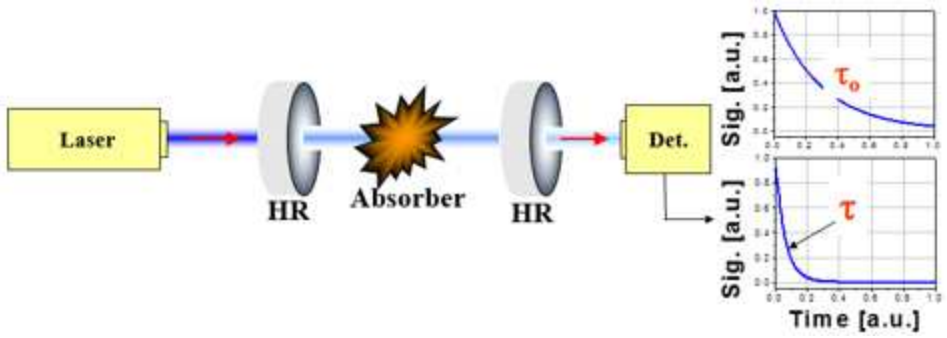

Figure 4. Schematic of a typical 2-mirror CRDS optical cavity with resulting ring-down decay profiles.

Our lab group has used CRDS in many studies related to ion propulsion, including sputtered metal surfaces [12], erosion studies of Hall thruster insulator channels [14–16], and a recent proof-of-principle using a lower power, heaterless BaO cathode [10]. Most recently, work using a CRDS diagnostic for cathode measurements using a higher-power (Mark II, 25 A class) cathode that is a component of the NASA's Advanced Electric Propulsion System (AEPS) has been completed, the cathode being described in work by Peterson et. al. [5]. This measurement has been made along the cathode axis by positioning the cathode to emit plasma toward the downstream mirror of the optical cavity, accessing the region within the cathode interior. Such a measurement is challenging due to the presence in the optical cavity of greater heat-loading, and radiative (and particle) fluxes, which can and often do degrade CRDS measurements. However, only measuring barium with the plasma plume would not provide the same understanding of the physics and plasma formation in the insert region, which is the primary focus of barium modeling efforts, making the increased experimental difficulty of barium measurements in the cathode interior worthwhile.

Overall, the barium work that is the focus of this thesis was done to support the modeling efforts of relevant 25A HC physics, such as barium transport modeling done by Polk et. al. [17]. The parameter studies of this work focus on cathode operating conditions that were used for

missions such as the HERMeS [18]. Here the parameters of interest of which barium density may be a function include the anode current used in the cathode-to-anode coupling, the flow rate of the krypton gas propellant, and cathode temperature, which is a function of both the current and flow parameters [19].

The rest of this thesis will focus on barium density measurements using CRDS. This work is followed by an appendix in which a laser diagnostic called two-photon laser induced fluorescence (TALIF) is used to measure krypton neutral densities in a cathode plume. TALIF will be introduced in the appendix introduction.

1.3 Thesis Objective

The main objective of this thesis is as follows: to develop a cathode testbed, that allows the necessary cathode conditioning and optical access; to build a robust CRDS optical cavity that allows consistent data collection; to enable barium density measurements within the HC plasma under various parameter conditions such as anode current and propellant flow rate, using CRDS. The rest of the thesis is laid out accordingly:

- Section two: give the CRDS optical setup, and the cathode mounting system
- Section three: state experimental results, including relevant parametric studies, including anode current and propellant flow, and compare results to relevant models
- In appendix, introduce TALIF and give the optical setup
- In appendix, show krypton TALIF measurements and krypton spatial mapping
- In appendix, discuss possible plume-to-spot mode transitions

Chapter 2- Experimental Setup

2.1 Optical Experimental Setup

The optical setup for the CRDS cathode measurements is shown below in Figure 5. Here the optical line of sight of the laser beam probes down the cathode hollow barrel. The dye laser is tuned to the region of the strong barium absorption line of 553.548 nm.

The laser beam used is generated with a dual laser system including a pump laser Nd:YAG (Continuum Powerlite 8010) that pumps the tunable dye laser mentioned above (Sirah CobraStretch). The CobraStretch uses a pyrromethene 580 dye (ethanol solvent). The laser output beam is ~2 mJ when leaving the dye laser, but is decreases to as low as ~70-100 μJ by the variable attenuator, which is composed of an iris to clean up any beam irregularities, a half-wave plate, and a polarizing cube. The laser energy is directed into the optical cavity with a periscope, since polarity is not critical to this study. The beam diameter is ~3-4 mm in diameter, which is sufficiently narrow for avoiding significant clipping on the interior diameter of the cathode, since the beam is fairly Gaussian in shape.

The optical cavity consists of the two ~99.99% reflective HR mirrors, which have a central reflectivity centered at 532 nm. The optical cavity is ~83.2 cm long, with this value including an extender arm ~16.5 cm long on the downstream side of the vacuum chamber. This arm creates a longer cavity, and also protects the HR mirror from plasma exposure and sputtered particles by creating a longer path for the plasma and particles to travel. The extender arm also proved protection to the mirror by providing room for the installation of two metal baffles with inner diameters of ~6 mm and ~10 mm, which collect plasma and contaminants while still allowing optical access. Since CRDS signals are weak due to the high reflectivity of the optical cavity, the

signal exiting the optical cavity must be magnified. In our case, the signal is detected with a photomultiplier tube (PMT, Hamamatsu R9110), which is operated with a gain of ~10^6. The presence of luminous plasma could easily overwhelm the signal, if not for the use of the wavelength passband (part) filter centered at 550 nm, with FWHM of 10 nm. To speed up the data collection and allow for quicker data monitoring, the CRDS signals are recorded by a custom LabVIEW program, in which log fitting of the ring-down time, τ, is provided for each laser shot, and each data collection is triggered by the photodiode that detects the split-off laser beam from an optical mirror. The data points are collected as the laser is tuned across the absorption line, with 50 waveforms collected and averaged, with the resulting ring-down then fitted to the resulting decay trace. In the data presented here, the dye laser is scanned from 553.536 nm to 553.562 nm, with tuning speed of 0.005 nm/minute.

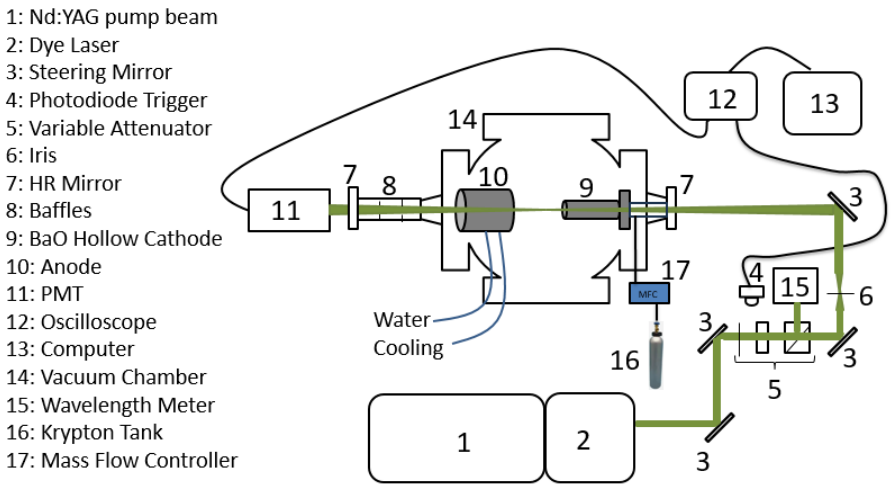

Figure 5. Optical layout of CRDS experiment. The CRDS optical axis is aligned along the centerline of the BaO HC with cavity high reflectivity (HR) mirrors surrounding the cathode.

2.2 HC Mount and Operating Conditions

Past work of our laboratory group has used a lower-power, heaterless BaO cathode for CRDS diagnostics, and further work using that cathode for TALIF will be mentioned in this work's appendix [10]. However, as mentioned above, the most relevant study for verifying modeling work is to use a mounting setup for the Mark II 25 A BaO HC that allows optical access down the axis of the cathode (see figure 6). The cathode is grounded, as the focus of this

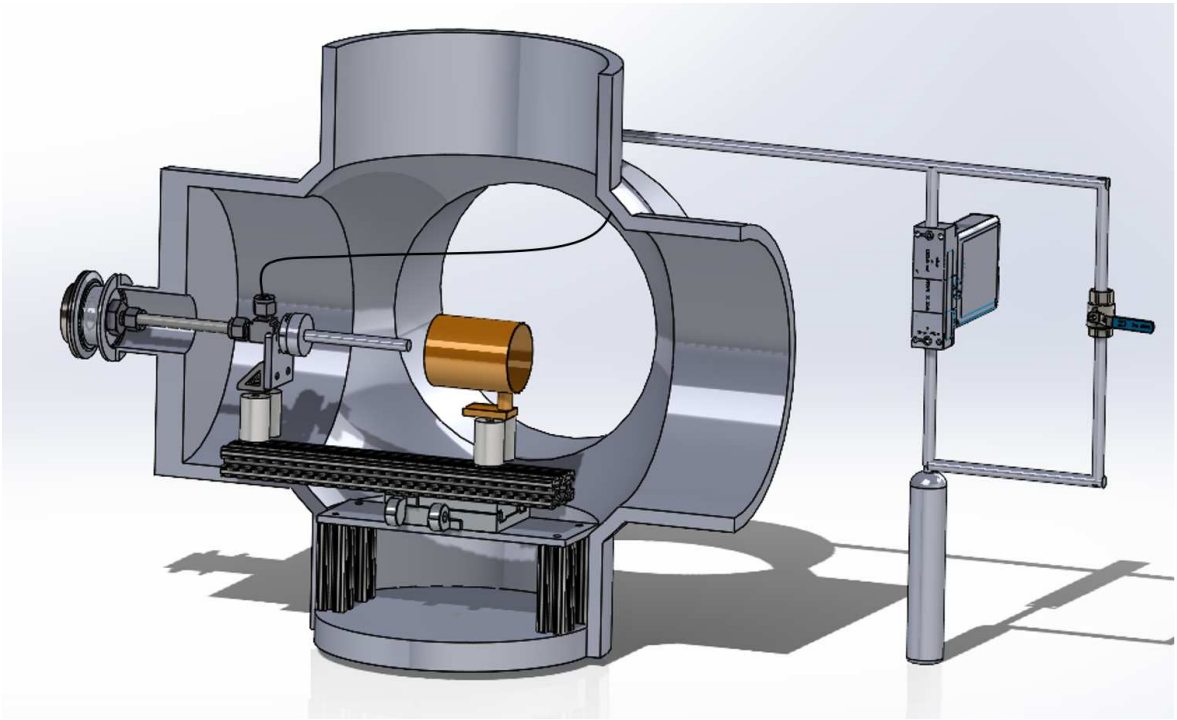

Figure 6. HC mounting system, vacuum chamber, HR mirror, and propellant flow system.

work is barium detection versus rigorously matching flight (floating) cathode conditions. In this mounting setup, the robustness of the cathode alignment is enhanced via adjustable HR mirror mounts. It is worth noting that aiming the plasma from this higher-current device directly at an HR mirror leads to great challenges in CRDS, that the previously mentioned jig, extender arm,

and adjustable HR mirrors cannot completely overcome. During the transition from empty cavity to plasma-on conditions, decreases as great as 4x in τ values have been seen.

A detailed view of the cathode mounting arrangement is as shown in Figure 7, with the green line showing the optical beam path, and barium densities measured along this path using the integrated techniques as stated in Section 1.2. There are three thermocouples spot-welded to three different locations on the outside of the cathode, inside the keeper, with one placed directly on the cathode orifice plate (TC1), one ~1 mm upstream (or towards the left in Figure 7) of the heater (TC2), and one in the middle of the cathode or approximately 15 mm upstream of the heater (TC3). The approximate axial locations of the thermocouples are indicated by the red crosses in Figure 7, but with the TCs actually within the keeper. During the experiments, TC1 encountered reliability issues due to the challenge of achieving good spot welds in such a high-temperature plasma environment, and TC3 did not give the highest (most relevant) temperatures due to its location further away from the plasma. TC2 was the thermocouple that gave the most consistent values, and therefore the temperature data in this work are measured using it.

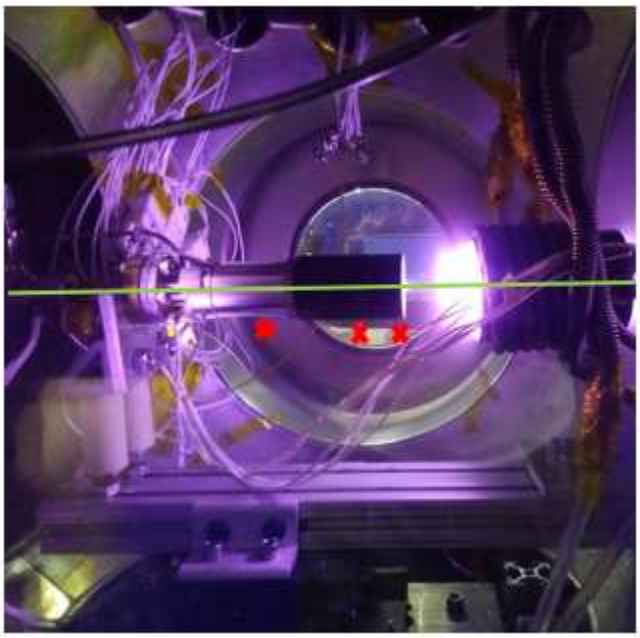

Figure 7. HC with running plasma, with green line representing the position of the CRDS laser beam. Red crosses show approximate axial location of the thermocouples, inside the keeper.

To help prevent cathode poisoning, the cathode was conditioned using the heater. Turning on heater currents of 3.85 and 7.20 A, for 3 and 1 hour, respectively, was done each time the cathode was brought down to vacuum.

In this work, several studies of barium density are conducted, with typical values of the heater current from 6-7.6 A, with voltages ~12-18 V; anode currents from ~5-25 A and voltages from ~20-38 V; and keeper currents from 0-1.7A, with voltages ~11-17 V. The pumps for the chamber include both a roughing pump and a turbomolecular pump (Agilent TV 1001). Using the turbomolecular pump at full power, the base pressure of the chamber is $\sim 10^{-6}$ torr, with a minimum value achieved of $\sim 10^{-7}$ torr, with operating pressures of $\sim 3 \times 10^{-4}$ torr when using the krypton propellant at flow rates considered in this work. The propellant is pure krypton, used since its properties are similar to xenon, and a mass flow controller (Brooks GF120) is used to control the flow rates of interest, ~5-40 sccm.

Chapter 3- Barium CRDS Results

3.1 Example Ba Spectrum and Ba Density Analysis

A sample spectra scan using the scan of the dye laser over the relevant wavelengths is shown in Figure 8. The target is again 553.548 nm, here given as normalized frequencies. The cathode is run only with the heater, at 7.6 A and no propellant flow, resulting in a clear absorption at the relevant frequency. Using equation (4), we are able to subtract the background and set a baseline as necessary. The empty cavity loss results in an absorbance of ~250 parts-per-million (ppm), corresponding to mirror R of ~0.99975. The baseline noise is ~5 ppm, due to the optical sensitivity of CRDS. Using the equations from section 1.2, the detection limits of achievable are 10^6-10^7 cm^{-3} (over an ~11 mm path length), based on the length of the maximum barium emission from modeling in Polk et. al [20]. Here the 11 mm path length is based on the maximum barium emission length from modeling results in the Polk et. al. work cited above.

An example of CRDS calculations as given in Section 1.2 is as follows: the area of the spectrum in Figure 8 is ~6.6×10^5 s^{-1}. Now using equation (5), a path-integrated Ba density of ~1.5×10^7 cm^{-2} can be found with the relevant spectroscopic constants. As stated, the path length can be assumed to be ~ 11 mm. So, the barium density is then found to be of ~1.4×10^7 cm^{-3}, and a uniform value over the path length must be assumed, since no mapping in the axial location is possible in this experiment. Observing the signal-to-noise to be ~10 in Figure 8, we can state the detection limit to be ~1×10^6 cm^{-3}.

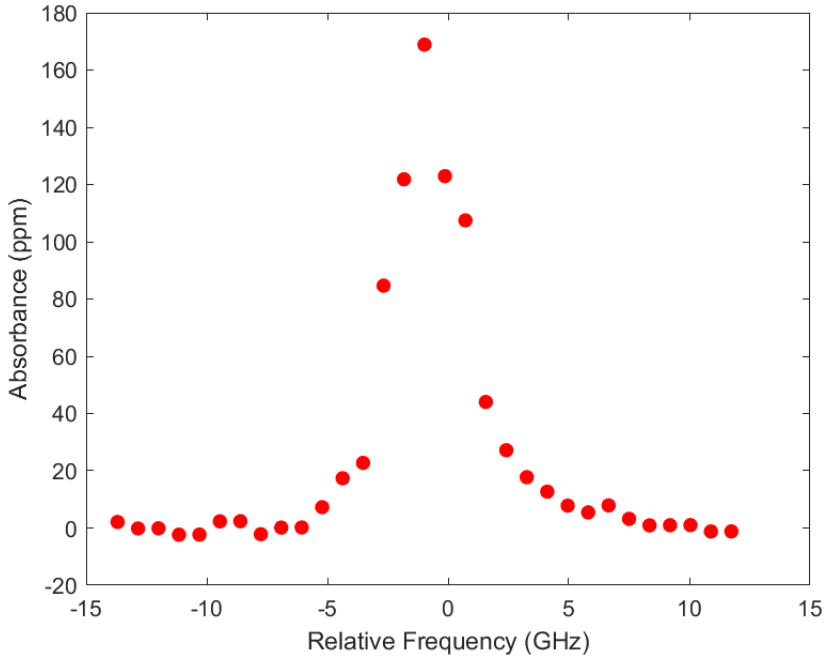

Figure 8. Barium absorption spectrum at 7.6 A heater current (no flow). Vertical axis is plotted as dimensional optical absorbance, in ppm, due to a single-pass of light through the cavity. The horizontal axis is relative frequency centered at the 553.548 nm resonance.

3.2 Ring-Down Acquisition During Cathode Operation

Having established the detection of barium using CRDS, some practical comments on CRDS signal acquisition during cathode operation are useful. Figure 9 shows a time-series of ring-down times collected during cathode conditioning. This is a heater-on, cathode plasma and anode-current-off condition, with the heater varying from 3.85 A to 7.2 A. The CRDS signal is consistent as the heating cycle begins and continues for ~5.5 hours, which included current-on and -off periods. Several user interventions occurred, which was important to improve the ring-down while the heater ran, with one significant drop at around 180 minutes that was fixed quickly with HR mirror adjustments. Here the turn-on of plasma is not shown, since the firing of the cathode in this particular experiment caused a significant drop in τ on the order of ~50% (which most likely was caused by a particle deposition on the HR mirrors), but in more recent keeper/cathode firing

sequences the issue has not been encountered, perhaps due to further conditioning of the cathode and/or better HR mirror positioning.

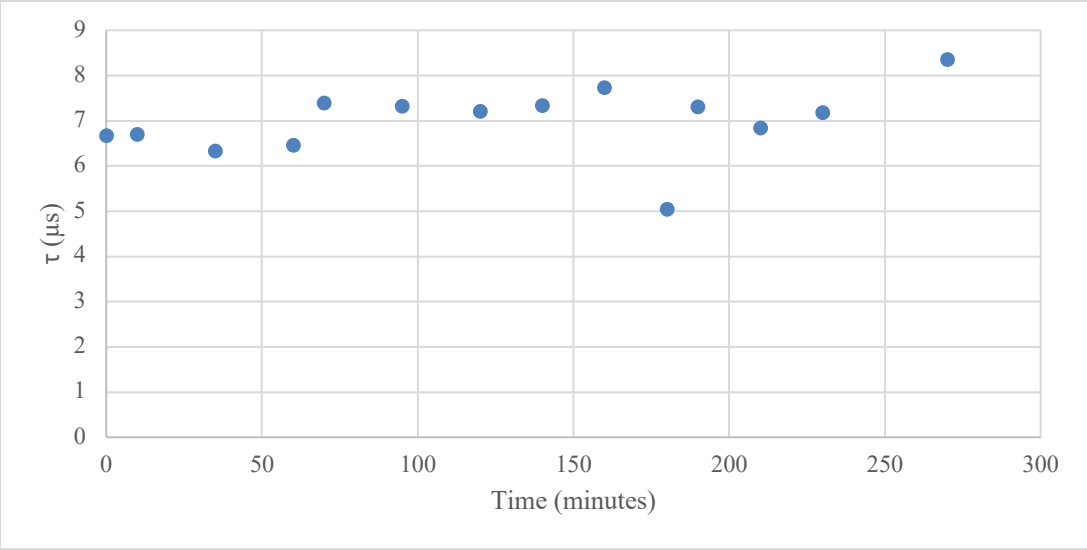

Figure 9. Stability of ring-down time over heating sequence, with sudden drop at around 180 minutes easily fixed by operator adjustment of HR mirror mounts.

3.3 Barium Density Dependence on Heater Current and Anode Current

The parameters most relevant to the ion propulsion community that affect HC barium density are current and propellant flow rate. Our first study shows barium density as function of heater current, as seen in Figure 10, noting that the temperatures of the cathode were ~769-938 °C as recorded by TC2. As expected, barium density increases as the current increases. The literature including work from Goebel et. al., and Hall et. al., indicates such a trend, in which anode current is positively correlated with cathode temperature, and barium emission is understood to be a positive function of cathode temperature [1,19]. It is noted that modeling work gives barium values ~10^{10} cm^{-3}, and the values reported here are three orders of magnitude smaller. A relevant consideration that may help explain this lack of agreement between experimental and modeling work is that the laser beam center is centered to the very middle of the on-axis location, and will

not be able to detect barium that does not transport out to the middle of the cathode barrel [20]. Barium values may be on the order of magnitude that is expected closer to the insert.

While most of the other studies in this work have 10% error, this heater study was less repeatable, and showed ~20% error. Also, the fit of the data trend matches literature including work from Crofton et. al. [9], which also exhibits an exponential trend.

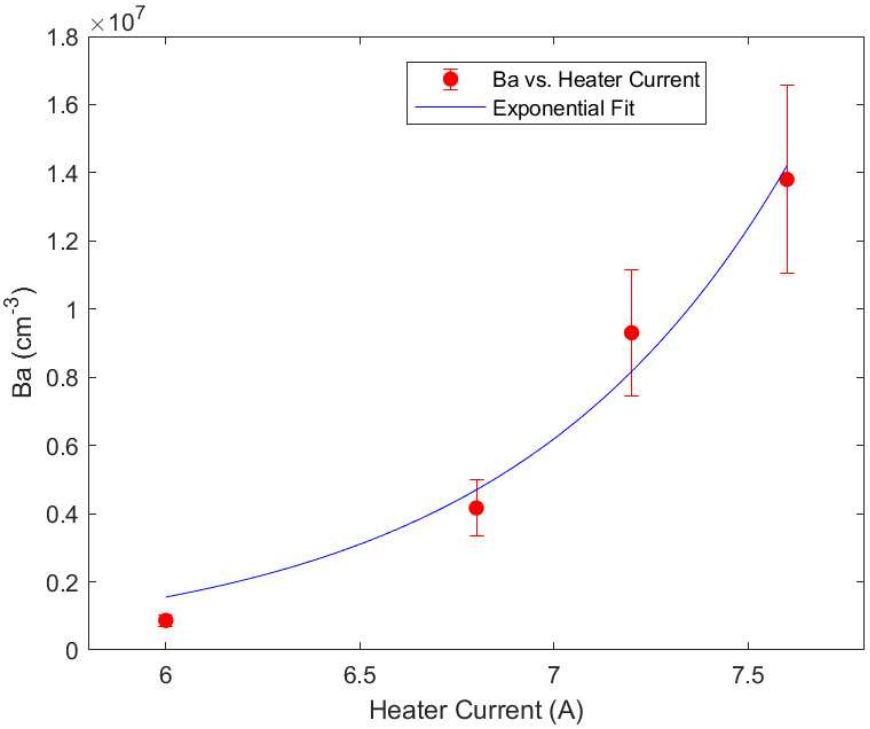

Figure 10. Barium density as a function of heater current (no flow).

Our second study was to leave the heater on at 7.6 A and step the keeper over increasing currents. As seen in Figure 11, the presence of keeper plasma correlated with lowered values of barium density, noting that the turn-on of current caused the largest drop in barium. It is likely that the lower barium values are caused by the ionization of the barium. We assign error bars of 10% for this study and throughout the rest of the barium work, based on experimental reproducibility.

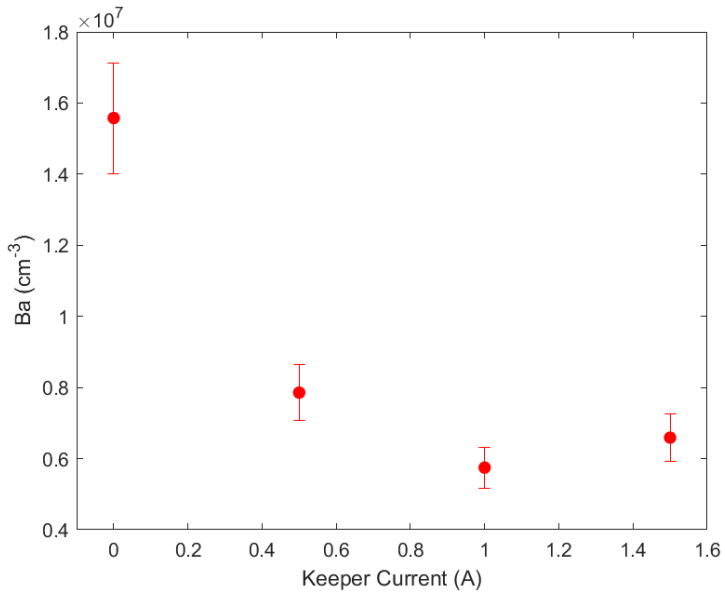

Figure 11. Barium density as a function of keeper current, with heater at 7.6 A

Our next study was to turn on the cathode via inducing a potential difference between the cathode and anode and observing the impact of varying the anode current and the corresponding barium density. In Figure 12, we see barium density traces as a function of anode current. Barium density shows a positive correlation to anode current, with the greatest increase in barium from current 20 A to 25 A.

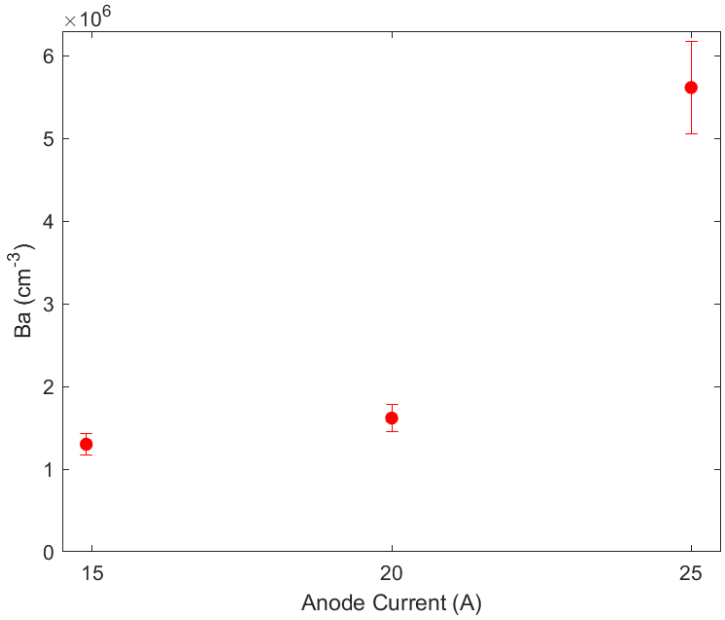

Figure 12. Barium density as a function of anode current at flow rate of 14.8 sccm.

In Figure 13, a study of barium density as a function of propellant flow rates is shown. Note that while the 20 A study was done sequentially, the 10 A study was done on different days,

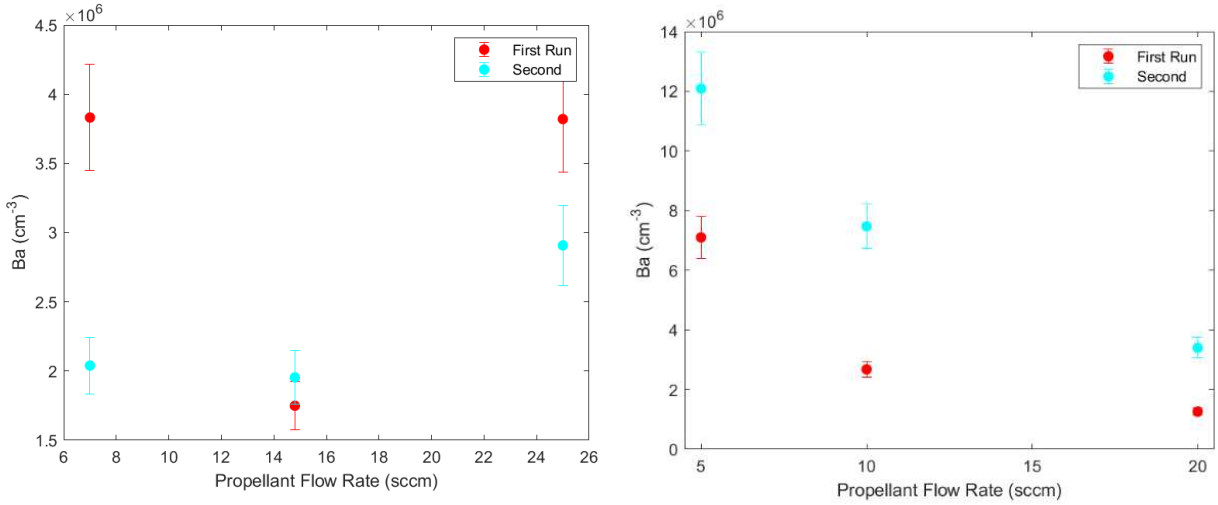

Figure 13. Barium as a function of propellant flow, with anode current as 20 A on the left, 10 A on the right.

but with otherwise nominally the same conditions. A clear downward trend is seen in the 10 A study, but not in the 20 A study. There is large disagreement at the 7 sccm flow condition for the 20 A study, but the 10 A study shows similar trends, indicating a possible inverse relationship between the flow and barium density.

It would be useful if our CRDS technique could give information from signal broadening, such as temperature values. In Figure 14 below, a comparison of FWHM of the signal with temperature from TC2 is given, but the opposite trend is found to what theory would suggest, in that higher temperatures should broaden signal.

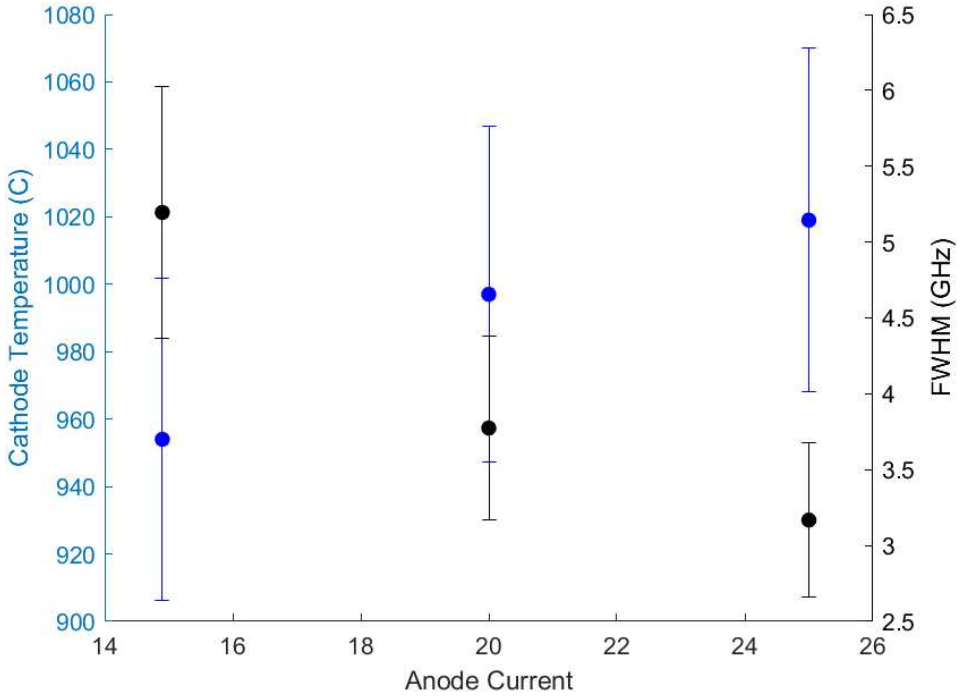

Figure 14. Comparison of cathode temperature and FWHM of signal over anode current trace. Inverse trend seen here.

In Figure 15, sample cathode performance metrics are plotted. We tracked the coupling voltage between the cathode and anode for various anode currents, revealing that with a current increase, the coupling voltage decreases slightly, matching with literature. In the literature, turning

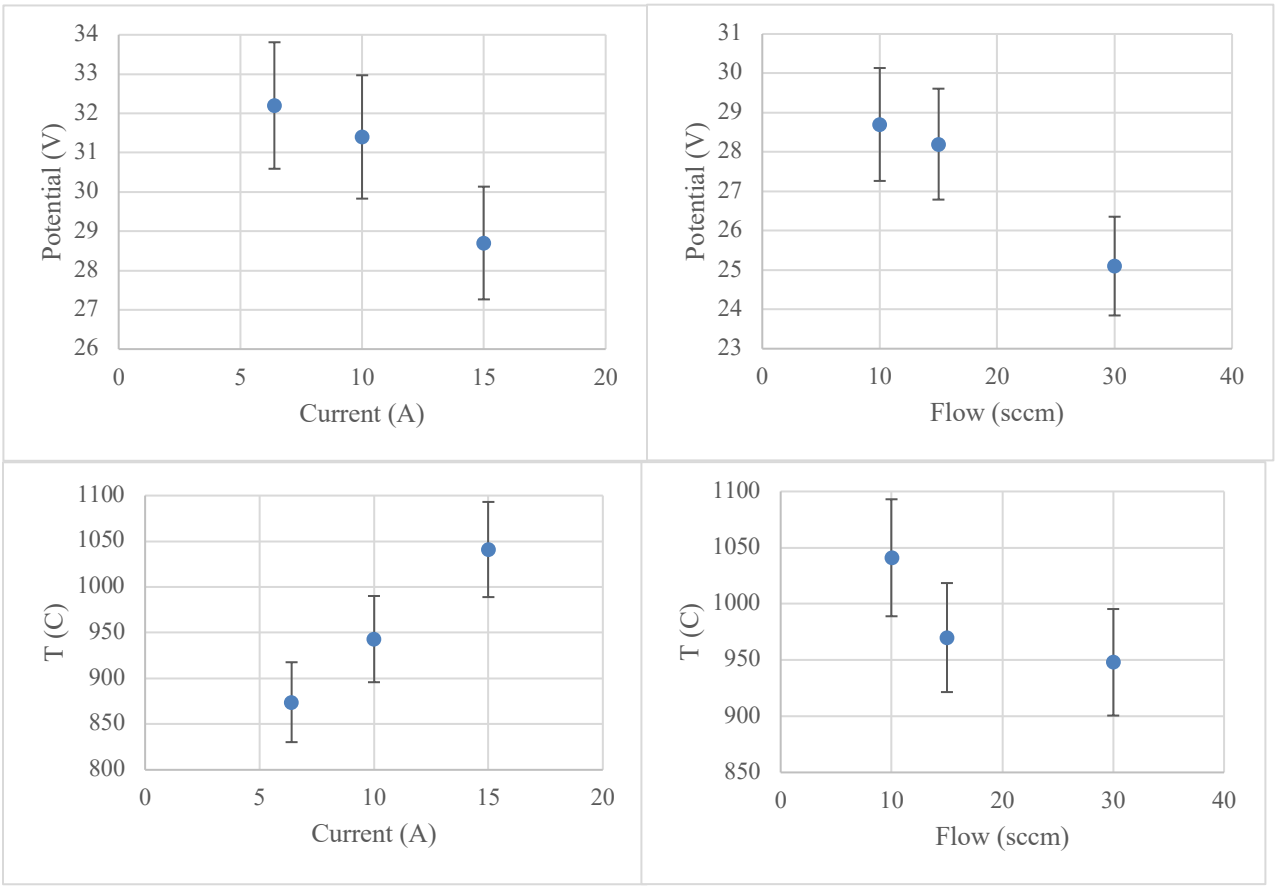

Figure 15. Cathode temperature and coupling potential as functions of propellant flow and anode current.

up anode current in the NSTAR cathode allows more electrons to overcome the voltage resistance of the cathode plasma sheath, which then correlates with lower plasma sheath voltages at that current condition [1]. When considering the coupling voltage as a function of propellant flow, higher flow enables increased coupling from cathode to anode. Also in Figure 15, the effect of anode current and propellant flow on cathode temperatures was tracked using thermocouple TC2. We find cathode temperature to be a positively correlated function of higher anode currents, and a negatively correlated function of flow rates, trends that match the literature as mentioned above [1,19,21].

Also interesting would be a further demonstration that plasma production ionizes barium and increases τ values, due to the reduction in barium absorption. Such a study may be done by setting the laser to the central barium absorption wavelength, and turning plasma on and off. In Figure 16 we see that as plasma is turned on, the τ value increases, although followed by a quick drop in τ as there are complications possibly due to both the addition of heat in the optical cavity, and greater quenching because of plasma in the cavity. When the plasma is turned off, τ drops as barium in the cavity increases. Then, since the cathode begins to rapidly cool and corresponding barium emission drops, τ increases, followed by the cathode heater being turned back on, leading to a gradual decrease in τ as cathode temperature and barium emission increases. With the heater off ~5 minutes after this experiment, τ is back at the nominal, no-barium τ value.

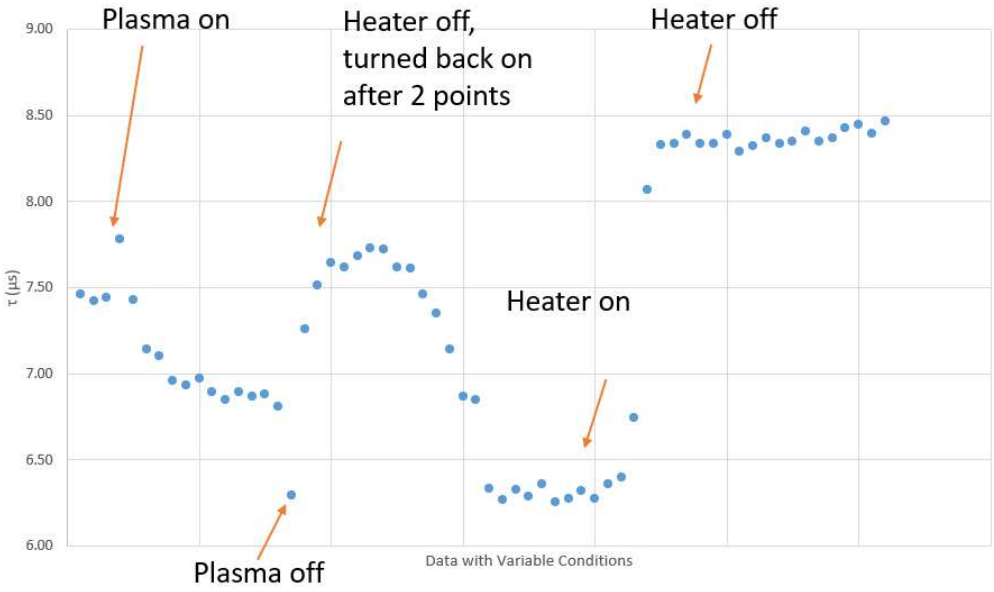

Figure 16. τ study as function of plasma condition (and barium presence).

It would be beneficial for future experiments if a characterization of barium density could be made from the difference between the baseline of our ring-down signatures and the minimum τ value. If τ as a value for a certain value of barium density could be found with confidence, the

time-intensive scans over the absorption feature could be avoided. Such a comparison is plotted in Figure 17, using the data from the anode current data trace in Figure 12.

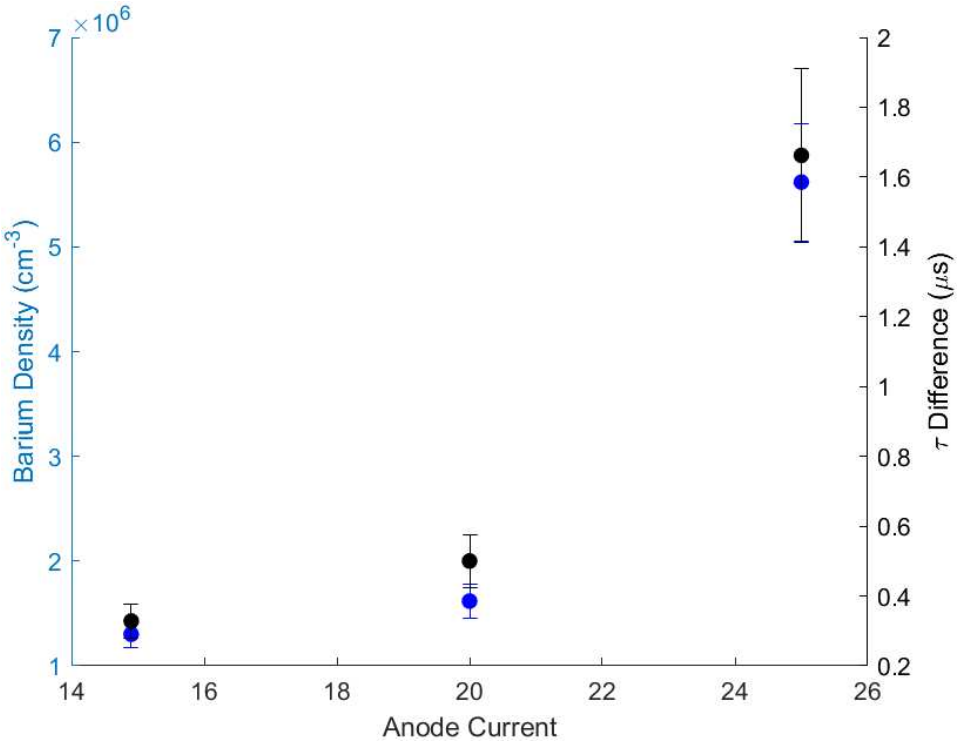

Figure 17. Traces of barium density and τ difference as functions of anode current.

Here we see that in this example, barium density and τ track well together, encouraging the possibility of future experiments being run with the laser parked at the central absorption wavelength, particularly if a barium density calibration device was built that is similar to the krypton reference cells used in TALIF krypton-detection studies done by our lab [22]. Note that the τ error bars are 15% since the repeatability of the τ difference is less than most of the data presented here.

Finally, the CRDS setup was utilized to attempt to detect ground state barium neutrals at a nearby absorption line of 551.904 nm [12]. Here, no barium was detected, likely due to the lower absorption coefficient of 5.7 10^7 [12]. The lack of absorption is seen in Figure 18, where the

theoretical detection limit of ~6.4 10^4 cm^{-3} is calculated based on the absorption feature that would match the data spread. Of course, this detection limit is ~1.5 orders magnitude lower than the theoretical detection limit reported in section 3.1, so care must be taken in basing decisions on this value. The width of the absorption is calculated using the typical FWHM of ~3 GHz found for much of the barium work.

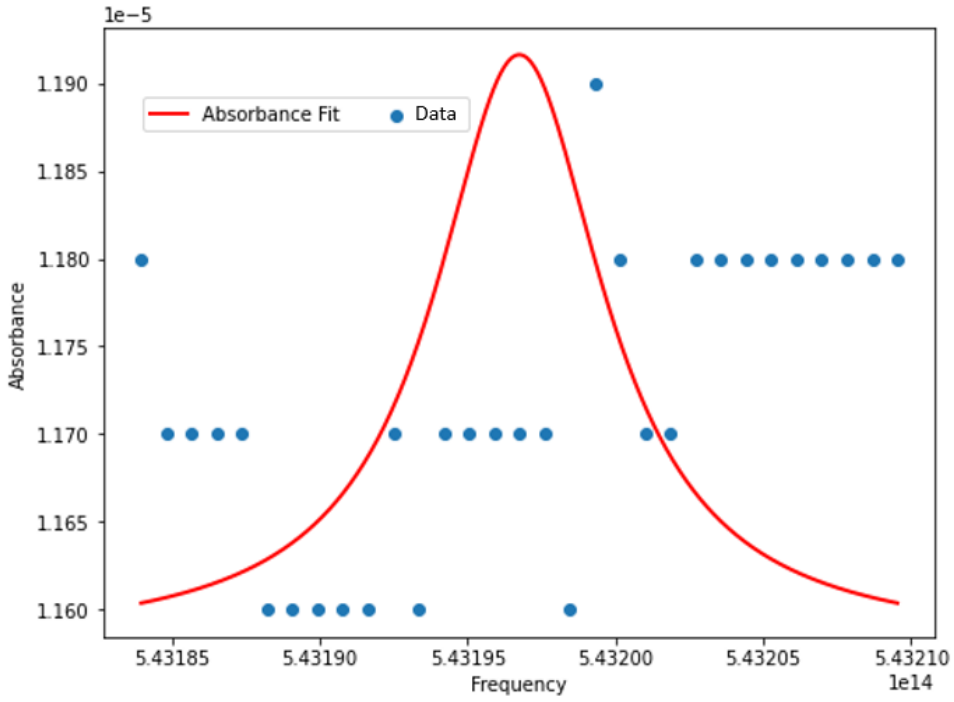

Figure 18. Data with only noise (no neutral barium) seen at 551.904 nm central scan. The absorbance fit allows a calculation of what barium density should be detectable.

3.4 CRDS Krypton Neutral Detection

In this last section, the detection of krypton neutrals using CRDS is discussed, at the wavelength of 552.118 nm. This is an extremely weak line, and the krypton is in an excited state, of 92,964 (cm^{-1}), or $4s^2 4p^5 (^2p^o_{3/2}) 5p$ [13]. Although calculating the krypton density in the same way that was done in the prior sections of Chapter 3 would be useful to our analysis, it is impossible currently because no Einstein coefficient is known for this absorption line.

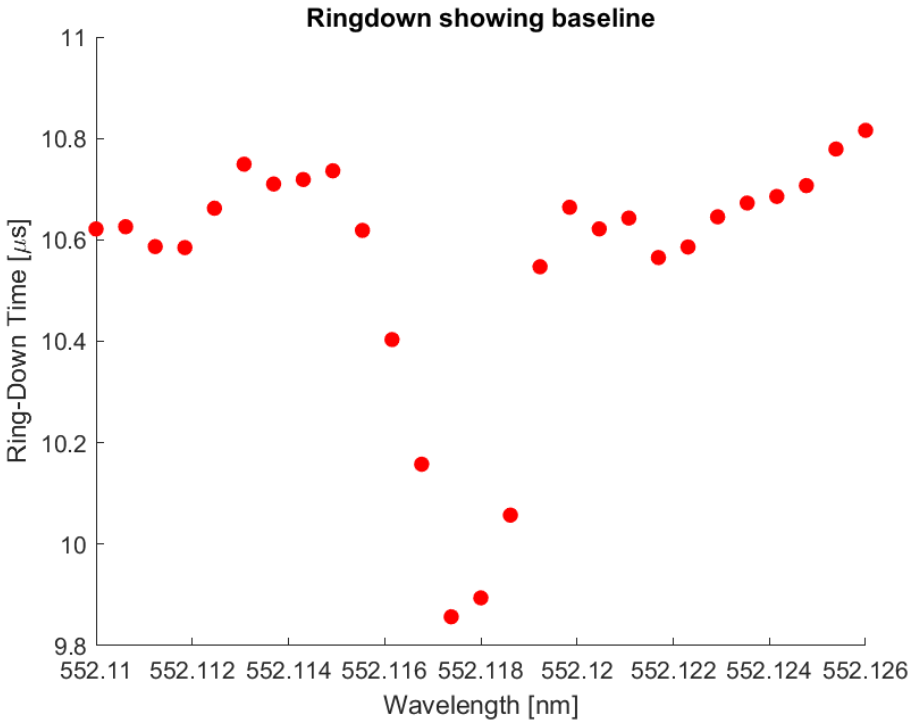

Figure 19. Absorbance plotted as function of wavelength scan over 552.118 nm, a weak absorption line for energized krypton.

Therefore, we will only give the absorption figure as shown here in Figure 19, in which the ring-down value drops as we tune the laser over the resonant wavelength. The cathode used is a heaterless, CSU Electric Propulsion and Plasma Engineering (CEPPE) designed cathode, and the probe beam enters the plasma in the outer plume only, due to the lack of optical line-of-sight, as mentioned in past papers such as our work presented in past conferences [10]. The cathode conditions are 5 A and 10 sccm krypton flow rate for this absorption feature.

3.5 Discussion

The focus of this thesis is on measurements of a Mark II 25 A cathode, both of barium density and performance data. Path-integrated measurements of barium are made along the optical path including within the interior of the cathode, enabling better understanding of the barium performance in the plasma in-line with the optical cavity. Experimental results at conditions

relevant to the ion propulsion community are given, including parameter studies for heater, keeper, and anode current, and also a propellant flow study.

The high sensitivity of the CRDS technique has been demonstrated, with a detection limit of species of ~10^6 cm^{-3}. Since temperature of the cathode is considered a proxy for barium density, and the temperature of the cathode positively correlates with higher anode currents, and drops with higher flow rates, we expect barium density to have similar relationships with these parameters. Overall, we do see these results. The propellant flow study is less repeatable at the constant 20 A anode current condition versus the 10 A anode current study. Work by Goebel and Hall does back up these results, as mentioned in section 3.3 [1,19]. One item of note is that some literature predicts barium densities on the order of ~10^8-10^{10} cm^{-3}, but in this study, data has shown densities considerably lower, ~10^7 cm^{-3} [17,20]. More work to understand the discrepancy is needed. Some potential issues could be as follows: the cathode may have reduced barium emission due to cathode lifetime [23], laser linewidth effects that will influence signals in pulsed-laser CRDS [24], and possible optical saturation (bleaching). Keeper current trends match well with work by Crofton et. al., although Crofton does report a peak barium density of ~1x10^9, two orders of magnitude greater than our peak value [9]. For the cathode performance metrics, the expected inverse relationship between anode potential and both current and propellant flow matches as shown in Goebel hold true, with higher currents allowing for emission of electrons with a lower cathode plasma sheath potential [1].

Chapter 4- Conclusion and Future Work

Overall, the CRDS diagnostic optical testbed shows its robustness as a species measurement tool in HC plumes. Work should continue to develop the diagnostic as a cathode-lifetime characterization tool, allowing potential simplifications of cathode preparation steps, such as reducing time-intensive bakeout procedures for the gas feedline, and shortening of the cathode conditioning process. This could be done by testing the effect of systematically eliminating steps of the preparation process, and observing any consequent variation in barium emission. In general, lower barium densities should signal a decrease in cathode lifetime. Perhaps such a diagnostic would allow a quantitative characterization of cathode barium emitter percentage of life remaining, which could be used as part of pre-flight test procedures.

Further tests with the Mark II 25 A cathode could include the following areas. Based on the sensitivity and robustness of the CRDS barium measurements, CRDS detection in the plume of the cathode mounted vertically would likely be effective, in that expected lower barium densities would still be detectable as plasma sputtering on the HR mirrors would be minimal compared to that present in the current down-barrel, horizonal mounting of the cathode. Mounting the cathode on a 2D stage would enable 2-D barium spatial maps, similar to prior krypton work from our lab [25]. Also, work in understanding barium densities during transitions to plume modes would be of interest. The author has qualitatively noted that operating at propellant-lean conditions such as 25 A and ~8 sccm or lower propellant flow may cause the cathode to enter a plume mode, but it is challenging to make barium measurements at such conditions since the background noise from plasma luminosity greatly increases, endangering the PMT [26]. Such work may be done by lowering the PMT setting and raising laser energy as necessary, although oversaturation of signal

may become a concern. Doing this study in a time-resolved manner and in concert with probe diagnostics would also be of interest, although the slow speed of barium spectral scans (~6 minutes) would create a challenge. Parking the laser at the resonant wavelength and using the resulting τ value would potentially obviate this issue, as long as high confidence is maintained in this measurement being truly representative of barium density. Measuring barium densities while including a magnetic field condition such as that found in a Hall thruster environment would be a logical next step. Finally, further work to measure the Ba^+ ion density could be done using a probe wavelength of 455.531 nm (vacuum) [13].

Bibliography

[1] Goebel, D. M., and Katz, I., "Fundamentals of Electric Propulsion: Ion and Hall Thrusters," California Institute of Technology, 2008.

[2] Brophy, J., "The Dawn Ion Propulsion System," *The Dawn Mission to Minor Planets 4 Vesta and 1 Ceres*, edited by C. Russell and C. Raymond, Springer New York, New York, NY, 2011, pp. 251–261. https://doi.org/10.1007/978-1-4614-4903-4_11

[3] Thomas, R., Patterson, M. J., John, J. W., and Crofton, M. W., "NEXT Ion Propulsion System Risk-Mitigation Tests in Support of the Double Asteroid Redirection Test (DART) Mission," presented at the AIAA Propulsion and Energy 2019 Forum, Indianapolis, IN, 2019. https://doi.org/10.2514/6.2019-4165

[4] Snyder, J. S., Goebel, D. M., Chaplin, V. H., Ortega, A. L., Mikellides, I. G., Aghazadeh, F., Johnson, I. k, and Kerl, T., "Electric Propulsion for the Psyche Mission," 2019.

[5] Peterson, P. Y., Herman, D. A., Kamhawi, H., Frieman, J. D., Huang, W., Verhey, T., Dinca, D., Boomer, K., Pinero, L., Criswell, K., Hall, S. J., Birchenough, A., Gilland, J. H., Hofer, R., Polk, J. E., Chaplin, V., Lobbia, R., Garner, C. E., and Kowalkowski, M. K., "Overview of NASA's Solar Electric Propulsion Project," presented at the 36th International Electric Propulsion Conference, Vienna, Austria, 2019.

[6] Simmons, N., "Experimental Comparison Between Hollow Cathodes with Cermet, Lanthanum Hexaboride, and Barium Oxide Insert Materials," Masters Theses. 3711., 2018.

[7] Gray, T. G., Haag, T., Sarver-Verhey, T. R., and Hall, S. J., "Effects of Environmental Exposure on Barium Oxide Cathode Operation," presented at the 37th International Electric Propulsion Conference, Cambridge, MA, USA, 2022.

[8] Coletti, M., and Gabriel, S. B., "A Model for Barium Oxide Depletion From Hollow Cathode Inserts," *IEEE Transactions on Plasma Science*, Vol. 37, No. 1, 2009, pp. 58–66. https://doi.org/10.1109/TPS.2008.2006898

[9] Crofton, M., "Measurement of Barium Production in a Hollow Cathode," presented at the 41st AIAA/ASME/SAE/ASEE Joint Propulsion Conference & Exhibit, Tucson, Arizona, 2005. https://doi.org/10.2514/6.2005-3665

[10] Antozzi, S., Gottfried, J., Williams, J., and Yalin, A. P., "Cavity Ring-Down Spectroscopy (CRDS) Measurements of Barium Emitted from a Hollow Cathode," presented at the AIAA SCITECH 2024 Forum, Orlando, FL, 2024. https://doi.org/10.2514/6.2024-0922

[11] Maity, A., Maithani, S., and Pradhan, M., "Cavity Ring-Down Spectroscopy: Recent Technological Advancements, Techniques, and Applications," *Analytical Chemistry*, Vol. 93, No. 1, 2021, pp. 388–416. https://doi.org/10.1021/acs.analchem.0c04329

[12] Yalin, A. P., Surla, V., Butweiller, M., and Williams, J. D., "Detection of Sputtered Metals with Cavity Ring-down Spectroscopy," *Appl. Opt.*, Vol. 44, No. 30, 2005, pp. 6496–6505. https://doi.org/10.1364/AO.44.006496

[13] Kramida, A., and Ralchenko, Y., "NIST Atomic Spectra Database, NIST Standard Reference Database 78," National Institute of Standards and Technology, 1999. https://doi.org/10.18434/T4W30F

[14] Dragnea, H. C., Boyd, I. D., Lee, B. C., and Yalin, A. P., "Characterization of Eroded Boron Atoms in the Plume of a Hall Thruster," *IEEE Transactions on Plasma Science*, Vol. 43, No. 1, 2015, pp. 35–44. https://doi.org/10.1109/TPS.2014.2320851
[15] Lee, B. C., Huang, W., Tao, L., Yamamoto, N., Gallimore, A. D., and Yalin, A. P., "A Cavity Ring-down Spectroscopy Sensor for Real-Time Hall Thruster Erosion Measurements," *Review of Scientific Instruments*, Vol. 85, No. 5, 2014, p. 053111. https://doi.org/10.1063/1.4879135
[16] Yamamoto, N., Tao, L., Rubin, B., Williams, J. D., and Yalin, A. P., "Sputter Erosion Sensor for Anode Layer-Type Hall Thrusters Using Cavity Ring-Down Spectroscopy," *Journal of Propulsion and Power*, Vol. 26, No. 1, 2010, pp. 142–148. https://doi.org/10.2514/1.44784
[17] Polk, J., Mikellides, I., Capece, A., and Katz, I., "Barium Depletion in Hollow Cathode Emitters," *Journal of Applied Physics*, Vol. 119, No. 2, 2009. https://doi.org/10.1063/1.4938489
[18] Sarver-Verhey, T. R., Kamhawi, H., Goebel, D. M., Polk, J. E., Peterson, P. Y., and Robinson, D. A., "Hollow Cathode Assembly Development for the HERMeS Hall Thruster," presented at the 52nd AIAA/SAE/ASEE Joint Propulsion Conference, Salt Lake City, UT, 2016. https://doi.org/10.2514/6.2016-5026
[19] Hall, S. J., Gray, T. G., Sarver-Verhey, T. R., and Kamhawi, H., "Emitter Surface Temperature Measurements of a 25-A Class Hollow Cathode," presented at the 37th International Electric Propulsion Conference, IEPC-2022-140, Cambridge, MA USA, 2022.
[20] Polk, J. E., Mikellides, I. G., Capece, A. M., and Katz, I., "The Effect of Cathode Geometry on Barium Transport in Hollow Cathode Plasmas," *Journal of Applied Physics*, Vol. 115, No. 18, 2014, p. 183301. https://doi.org/10.1063/1.4873168
[21] Goebel, D., "Extending Hollow Cathode Life for Electric Propulsion for Long-Term Missions," presented at the Space 2004 Conference and Exhibit, San Diego, California, 2004. https://doi.org/10.2514/6.2004-5911
[22] Gottfried, J., Antozzi, S., Stienike, J., Thompson, S., Williams, J., and Yalin, A. P., "Temporally Resolved Neutral Density Measurements of Hall Effect Thruster Breathing Mode by Two-Photon Absorption Laser Induced Fluorescence (TALIF)," presented at the AIAA SCITECH 2024 Forum, Orlando, FL, 2024. https://doi.org/10.2514/6.2024-0802
[23] Polk, J. E., Goebel, D., Brophy, J. R., Beatty, J., Monheiser, J., Giles, D., Hobson, D., Wilson, F., Christensen, J., De Pano, M., Hart, S., Ohlinger, W., Hill, D. N., Williams, J., Wilbur, P., Laufer, D. M., and Farnell, C., "An Overview of the Nuclear Electric Xenon Ion System (NEXIS) Program," presented at the AIAA-2003-4713, Huntsville, AL, 2003.
[24] Yalin, A., and Zare, R., "Effect of Laser Lineshape on the Quantitative Analysis of Cavity Ring-Down Signals," *Laser Physics*, Vol. 12, No. 8, 2002. https://www.researchgate.net/publication/246019716_Effect_of_Laser_Lineshape_on_the_Quantitative_Analysis_of_Cavity_Ring-Down_Signals
[25] Antozzi, S., Gottfried, J., Williams, J. D., and Yalin, A. P., "Spatially Resolved Measurements of Krypton by Two-Photon Absorption Laser Induced Fluorescence (TALIF) in a Barium Oxide Hollow Cathode Plasma," presented at the AIAA AVIATION 2023 Forum, San Diego, CA and Online, 2023. https://doi.org/10.2514/6.2023-4269
[26] Mikellides, I. G., Guerrero, P., Lopez Ortega, A., and Polk, J. E., "Spot-to-Plume Mode Transition Investigations in the HERMeS Hollow Cathode Discharge Using Coupled 2-D

Axisymmetric Plasma-Thermal Simulations," presented at the 2018 Joint Propulsion Conference, Cincinnati, Ohio, 2018. https://doi.org/10.2514/6.2018-4722
[27] Kim, V., Popov, G., Arkhipov, B., Murashko, V., Gorshkov, O., Koroteyev, A., Garkusha, V., Semenkin, A., and Tverdokhlebov, S., "Electric Propulsion Activity in Russia," presented at the 27th International Electric Propulsion Conference, IEPC-01-05., Pasadena, CA, 2001.
[28] "NASA - Ion Propulsion," NASA Space Tech, Jan 11 2016. Retrieved 9 November 2022. https://www.nasa.gov/centers/glenn/about/fs21grc.html
[29] Brophy, J. R., "NASA's Deep Space 1 Ion Engine (Plenary)," *Review of Scientific Instruments*, Vol. 73, No. 2, 2002, pp. 1071–1078. https://doi.org/10.1063/1.1432470
[30] Coletti, M., and Gabriel, S., "A Chemical Model for Barium Oxide Depletion from Hollow Cathode's Insert," *43rd AIAA/ASME/SAE/ASEE Joint Propulsion Conference & Exhibit*, American Institute of Aeronautics and Astronautics, 2007. https://doi.org/10.2514/6.2007-5193
[31] Williams, J. D., and Wilbur, P. J., "Electron Emission from a Hollow Cathode-Based Plasma Contactor," *Journal of Spacecraft and Rockets*, Vol. 29, No. 6, 1992, pp. 820–829. https://doi.org/10.2514/3.25537
[32] I. G. Mikellides, D. M. Goebel, B. A. Jorns, J. E. Polk, and P. Guerrero, "Numerical Simulations of the Partially Ionized Gas in a 100-A LaB6 Hollow Cathode," *IEEE Transactions on Plasma Science*, Vol. 43, No. 1, 2015, pp. 173–184. https://doi.org/10.1109/TPS.2014.2320876
[33] Dietz, P., Gärtner, W., Koch, Q., Köhler, P. E., Teng, Y., Schreiner, P. R., Holste, K., and Klar, P. J., "Molecular Propellants for Ion Thrusters," *Plasma Sources Science and Technology*, Vol. 28, No. 8, 2019, p. 084001. https://doi.org/10.1088/1361-6595/ab2c6c
[34] Nakles, M., Hargus, W., Delgado, J., and Corey, R., "A Performance Comparison of Xenon and Krypton Propellant on an SPT-100 Hall Thruster," presented at the 32nd International Electric Propulsion Conference, Weisbaden, Germany, 2011. https://doi.org/IEPC-2011-003
[35] Lingwei, Z., Yu, L., Juan, L., Zuo, G., Haocheng, J., Haixing, W., and Haibin, T., "Numerical Simulation of Characteristics of CEX Ions in Ion Thruster Optical System," *Chinese Journal of Aeronautics*, Vol. 23, No. 1, 2010, pp. 15–21. https://doi.org/10.1016/S1000-9361(09)60182-5
[36] Young, C. V., Fabris, A. L., MacDonald-Tenenbaum, N. A., Hargus, W. A., and Cappelli, M. A., "Time-Resolved Laser-Induced Fluorescence Diagnostics for Electric Propulsion and Their Application to Breathing Mode Dynamics," *Plasma Sources Science and Technology*, Vol. 27, No. 9, 2018, p. 094004. https://doi.org/10.1088/1361-6595/aade42
[37] Mazouffre, S., Kulaev, V., and Luna, J. P., "Ion Diagnostics of a Discharge in Crossed Electric and Magnetic Fields for Electric Propulsion," *Plasma Sources Science and Technology*, Vol. 18, No. 3, 2009, p. 034022. https://doi.org/10.1088/0963-0252/18/3/034022
[38] Eichhorn, C., Pietzonka, L., Scholze, F., Bundesmann, C., Spemann, D., Neumann, H., and Leiter, H. J., "Single- and Two-Photon Absorption Laser-Induced Fluorescence Spectroscopy in Rare Gases for Gridded Ion Thruster Diagnostics," *EPJ Techniques and Instrumentation*, Vol. 9, No. 1, 2022, p. 2. https://doi.org/10.1140/epjti/s40485-022-00077-y

[39] Wegner, J. T., “Two-Photon Absorption Laser Induced Fluorescence (TALIF) of Neutral Xenon in a Hall Effect Thruster Plasma,” M.S. Colorado State University, Fort Collins, CO, 2021.
[40] Kinefuchi, K., Nunome, Y., Cho, S., Tsukizaki, R., and Chng, T. L., “Two-Photon Absorption Laser Induced Fluorescence with Various Laser Intensities for Density Measurement of Ground State Neutral Xenon,” *Acta Astronautica*, Vol. 161, 2019, pp. 382–388. https://doi.org/10.1016/j.actaastro.2019.03.018
[41] Tango, W. J., Link, J. K., and Zare, R. N., “Spectroscopy of K2 Using Laser-Induced Fluorescence,” *The Journal of Chemical Physics*, Vol. 49, No. 10, 1968, pp. 4264–4268. https://doi.org/10.1063/1.1669869
[42] Steinberger, T., “Single and Multi-Photon Laser Induced Fluorescence for Electric Thruster and Fusion,” 2021.
[43] Wegner, T., Yalin, A. P., and Dumitrache, C., “Rate-Equation Modeling of Xe and Kr TALIF for Electric Propulsion Applications,” presented at the 37th International Electric Propulsion Conference, Cambridge, MA, 2022.
[44] Crofton, M., “Measurement of Neutral Xenon Density Profile in an Ion Thruster Plume,” *27th Plasma Dynamics and Lasers Conference*, American Institute of Aeronautics and Astronautics, 1996. https://doi.org/10.2514/6.1996-2290
[45] Eichhorn, C., Winter, M., Auweter-Kurtz, M., and Löhle, S., “Multi-Photon Spectroscopy on Xenon for Application on Ion Thruster Plasma Parameter Investigations: Experiment and Theory,” 2007.
[46] Crofton, M. W., Hsu Schouten, A. G., Young, J. A., Beiting, E. J., Diamant, K. D., Corey, R. L., and Delgado, J. J., “Neutral Xenon Density in the SPT-140 Near-Field Plume,” presented at the 33rd International Electric Propulsion Conference, Washington D. C., 2013.
[47] Wegner, T., Thompson, S. J., Williams, J., and Yalin, A. P., “Two-Photon Absorption Laser Induced Fluorescence (TALIF) Of Neutral Xenon In A Hall Effect Thruster Plasma,” 2021. https://doi.org/10.2514/6.2021-3391
[48] Gottfried, J., Antozzi, S., Dumitrache, C., and Yalin, A., “Preliminary Krypton Measurements by Two-Photon Absorption Laser Induced Fluorescence (TALIF) in Cold Flow and a Hollow Cathode Plasma,” 2023. https://doi.org/10.2514/6.2023-1863
[49] Shekhtman, D., Parziale, N. J., and Mustafa, M. A., “Excitation Line Optimization for Krypton Tagging Velocimetry and Planar Laser-Induced Fluorescence in 200-220 Nm Range,” presented at the AIAA Scitech 2021 Forum, VIRTUAL EVENT, 2021. https://doi.org/10.2514/6.2021-1300
[50] Grib, S. W., Jiang, N., Hsu, P. S., Stauffer, H. U., Felver, J. J., Roy, S., and Schumaker, S. A., “100 kHz Krypton-Based Flow Tagging Velocimetry in a High-Speedflow,” *Applied Optics*, Vol. 60, No. 6, 2021, pp. 1615–1622. https://doi.org/10.1364/AO.415976
[51] Magee, R. M., Galante, M. E., McCarren, D., Scime, E. E., Boivin, R. L., Brooks, N. H., Groebner, R. J., Hill, D. N., and Porter, G. D., “A Two Photon Absorption Laser Induced Fluorescence Diagnostic for Fusion Plasmas,” *Review of Scientific Instruments*, Vol. 83, No. 10, 2012, p. 10D701. https://doi.org/10.1063/1.4728092
[52] Ham, R. K., “AN EXPERIMENTAL INVESTIGATION OF HEATERLESS HOLLOW CATHODE IGNITION,” Colorado State University, 2020.

[53] Becatti, G., Goebel, D. M., Yoke, C. V., Ortega, A. L., and Mikellides, I. G., "High Current Hollow Cathode for the X3 100-kW Class Nested Hall Thruster," presented at the IEPC-2019-371, 2019.
[54] Jameson, K., Goebel, D., Mikellides, I., and Watkins, R., "Local Neutral Density and Plasma Parameter Measurements in a Hollow Cathode Plume," presented at the 42nd AIAA/ASME/SAE/ASEE Joint Propulsion Conference & Exhibit, Sacramento, California, 2006. https://doi.org/10.2514/6.2006-4490
[55] Goebel, D. M., Becatti, G., Mikellides, I. G., and Lopez Ortega, A., "Plasma Hollow Cathodes," *Journal of Applied Physics*, Vol. 130, No. 5, 2021, p. 050902. https://doi.org/10.1063/5.0051228

Appendix: Spatially Resolved Krypton Neutral Measurements using Two-Photon Absorption Laser Induced Fluorescence (TALIF)

A.1 Introduction

The main section of this thesis focused on barium density measurements in the plasma plume of a 25 A HC. It is also worth discussing the densities of other neutral species in the plasma plume of a HC, namely the density of krypton neutrals in a krypton-fueled cathode. This appendix gives such a study.

As mentioned in the introduction, electric thrusters are used for many applications, from satellite keeping [1,27] to deep-space exploration missions [1,28,29]. The low fuel mass and high specific impulse [1] enable long missions [29]. The importance of HCs for HETs has been mentioned in the introduction, with much research done in this area to model relevant physics and performance [17,30–32].

Xenon has been the propellant of choice for ion propulsion, since noble gases are inert, and xenon specifically is high in mass [33]. With the recent increases in xenon cost, there is a need for further data on ion propulsion devices that run on krypton instead, as that is an increasingly common propellant gas of choice. This substitution causes small decreases in performance, with one study finding an 8% decrease in thrust efficiency for a SPT-100 HET run on krypton [34]. Many models within the ion propulsion community need neutral propellant number density values as an input to the model, and there is a limited amount of data with krypton as the propellant. Focusing on the spatial density distribution of neutral krypton atoms within the plume region downstream of the HC orifice is important for characterizing model performance, as the results give greater understanding of propellant utilization and charge-exchange reactions (CEX), which

are the collisions of neutrals and ionized particles. There are two main reasons for modeling CEX reactions: measuring ion back-streaming [35] and sputtering, both of which can decrease device lifetime.

As mentioned in the introduction, laser diagnostics are an excellent choice for plasma diagnostics due to low perturbation of the plasma, and ability to probe difficult regions. Laser Induced Fluorescence (LIF) is a common diagnostic within ion propulsion, for such uses as velocity distributions [36,37]. To introduce the diagnostic, LIF uses a laser probe beam to excite an electron of the target atom to a higher energy, which electron then de-excites, emitting radiation. This radiation emission is detectable as a fluorescence signal [38,39]. For studies relevant to propellant characterization, such as this work, measurement of the ground state energy level of krypton neutrals is of most interest. However, the proper wavelength for accessing these energy gaps for krypton neutrals would need very high-energy, low-wavelength lasers (~100-125 nm), which are not commercially available [38]. A solution to this issue is to use Two-photon Absorption Laser Induced Fluorescence (TALIF).

A bit of history and background on TALIF follows: Richard Zare was the first to demonstrate TALIF in 1968. TALIF excites the atom of interest with two simultaneous photons to achieve the needed transition from the ground state such that (available) longer wavelength (~200-250 nm) lasers can be used [40–43]. The body of research using TALIF on ion propulsion devices includes approximately three decades of work, such as a study in 1996 by Crofton, which found that a 225.4 nm TALIF excitation scheme successfully detected xenon neutrals in the axial direction within the plasma of a T5 thruster, to the order of $10^{17}m^{-3}$ [44]. Another set of studies from Eichhorn et. al., has recently used 224.2 nm, 226.4 nm, and 225.4 nm schemes in xenon cold flow [45]. More work from Crofton performed a radial and axial study of xenon neutrals in the

plume of a Hall thruster in 2013 [46]. Recent work from our lab group successfully detected xenon neutrals with a 222.5 nm TALIF scheme in a Hall Thruster plume, and krypton neutrals using a 214.7 nm TALIF scheme in a BaO HC [47,48]. Further work by the Eichhorn group has mapped neutral densities of krypton in the plume of a gridded ion thruster with a TALIF scheme of 212.6 nm [38]. Recent work by our lab group focuses on characterizing breathing modes for Hall thrusters using TALIF in a temporally-resolved scheme [22].

In this thesis appendix, TALIF is further developed for krypton applications by using the 212.6 nm excitation scheme to achieve 2-D spatial mapping of atomic, neutral krypton within the plasma plume of a BaO HC, work that is detailed in Antozzi et. al. [25]. The rest of the study in this appendix is laid out as follows: A.2: Experimental Setup, A.3: Results, and A.4: Discussion.

A.2 Experimental Setup

A.2.1 Optical Setup and Excitation Schemes

To generate the probe beam for this study, we use two lasers, a pump of the third harmonic output of a Nd:YAG laser (Spectra-Physics Quanta Ray) directed into a dye laser (Sirah PrecisionScan), that creates a tunable wavelength beam using Exalite 428 dye. The output is doubled by a beta barium borate (BBO) crystal to ~212.6 nm, with resulting energy values up to 4 mJ. The laser output is directed through an anti-reflection window (TP01926060) into the vacuum chamber as shown in Figure 20. Creating a beam focus is helpful so that the location of greatest krypton excitation is identifiable as a collection volume, so a 500 mm plano-convex lens is used to weakly focus the laser probe. The lens is placed directly outside the vacuum chamber with the beam waist located approximately in the center of the chamber, centered directly underneath the HC plate orifice. The resulting fluorescence signal of 758.7 nm is collected with a convex-convex lens (Newport KBX160AR.16), along with the plasma luminous emission. This signal is fiber

coupled with a 600 micron fiber-optic cable, and directed onto a Hamamatsu R3896 photo-multiplier tube (PMT), the ratio of the image mapped onto the PMT being 1:1. This fiber-coupling system allows for reduction of luminosity collection to avoid poor SNR and potential PMT damage. For this work, we set the PMT to ~600 volts, which results in gain of ~$2x10^5$. This setting maximized signal strength without oversaturating the PMT [48]. Since the plasma luminosity is quite strong, the fluorescence is filtered with a bandpass filter (Thorlabs FHB760-10).

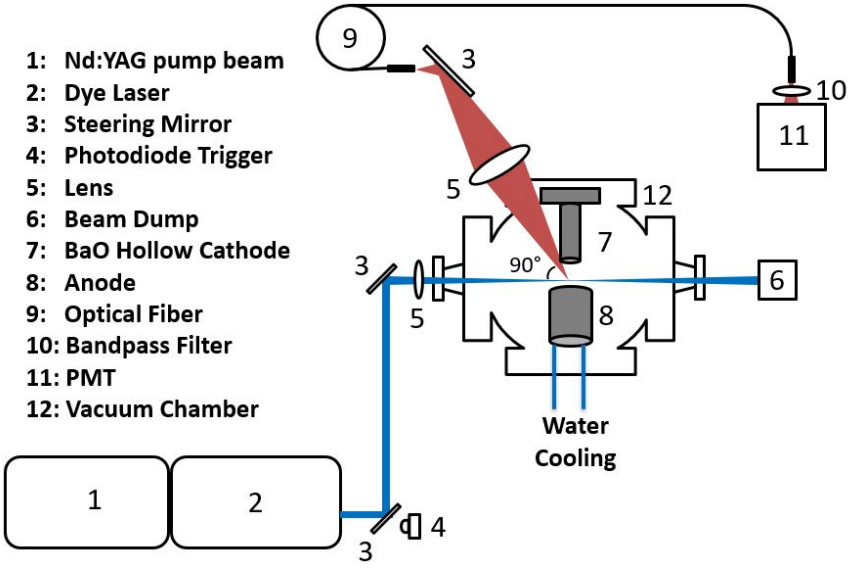

Figure 20. Optical Layout for TALIF.

The cathode setup is as follows: a high-current, heaterless BaO cathode that is custom-built by the Center for Electric Propulsion and Plasma is used, vertically mounted on a two-dimensional translation stage allowing for sub-millimeter movements in both the axial and radial directions of the HC output. The cathode krypton flowrates in this study are in the range 3 – 15 SCCM, and are controlled by a mass flow controller (Celerity Unit UFC-7360). The experiment required two high-current power supplies (Sorensen DCS 600-1.7 for the keeper, and a 13 A power supply for the anode) to power the cathode, set to constant current operation and floating voltages. The cathode is ungrounded. The BaO cathode currents in this study are between 5 and 13 A. Our vacuum

chamber is approximately spherical, and has dimensions of 60 cm x 60 cm x 60 cm. The pump used is an Agilent TV 1001 turbomolecular pump, achieving base pressures of ~10^{-6} torr. When experiments are done at krypton flowrates ~3-15 sccm as done for the data in this appendix, the chamber will reach pressures of ~0.5 mTorr.

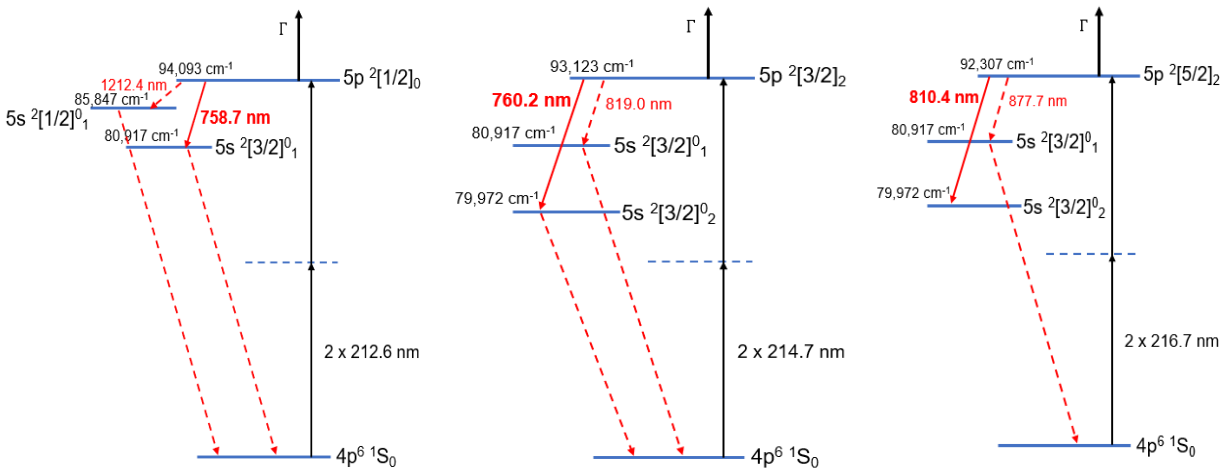

Figure 21. TALIF Pumping Schemes [47].

The krypton TALIF excitation schemes are shown in Figure 21 above. The scheme in the figure on left, namely 212.6 nm, is the excitation scheme that is used for most of the work in this appendix. To track the krypton electron excitation, the electron begins at the base level $4p^6\ ^1S_0$, then is excited by the TALIF pulse to the $5p\ ^2[1/2]_0$ level. The decay to the $5s\ ^2[3/2]^0_1$ level produces the TALIF signal of 758.7 nm which is the basis of our TALIF signal. The 214.7 scheme shown in the figure on the right was used in prior work by our lab group for TALIF neutral sensing of krypton, and is briefly used in this study for a flow rate comparison (Fig. 4) [48]. Part of this excitation is the same as the 212.6 scheme, with the krypton electron beginning at the base level $4p^6\ ^1S_0$, but then is excited to a different level, namely $5p\ ^2[3/2]_2$. Decaying to the $5s\ ^2[3/2]^0_2$ level produces the TALIF signal of 760.2 nm.

The data collection for this study was collected by the PMT mentioned above and then read into the computer, where the signal was integrated using a custom Labview code. The dye laser wavelength was tuned to the setting that gave the peak TALIF signal. Since there is a fair amount of noise from plasma, it is desirable to maximize the signal to noise ratio. Therefore, the integrated TALIF signal is averaged over 500 shots, based on a SNR study in previous work from our lab group [48].

A.2.2 Excitation Scheme Comparison

Krypton has several excitation lines regimes, with the three most commonly used being 212.6 nm, 214.7 nm, and 216.7 nm. These wavelengths are favored due to their strong excitation energy and compatibility with commercially available lasers [49]. According to Shekhtman's research, the 212.6 nm line is anticipated to produce the most intense peak TALIF signal [43,49,50]. As shown in Figure 22, the 212.6 nm scheme yields an average signal approximately five times stronger than the 214.7 nm scheme. This finding is consistent with our previous lab work, which indicated that the 212.6 nm scheme should produce a signal about seven times greater than the 214.7 nm scheme, thereby supporting the choice of the 212.6 nm wavelength excitation regime for this study [43].

In Figure 22, the TALIF signals for all three excitation schemes are depicted. The 212.6 nm scheme shows a relatively linear increase in signal up to 1.4 mJ, after which it experiences a gradual roll-off until ~3.2 mJ, followed by a plateau and slight decrease. This analysis highlights the 216.7 nm scheme and show pronounced saturation effects compared to past work from our lab [51].

The 216.7 nm scheme produces weaker signals, partly due to lower detector responsivity at 810 nm and reduced transmission through the bandpass filter. Energy error bars of 0.1 mJ reflect laser energy fluctuations, while TALIF signal error bars of 10% account for reproducibility issues stemming from laser energy variations, frequency-tuning drift of the dye laser, and potential minor variations in the cathode flow field.

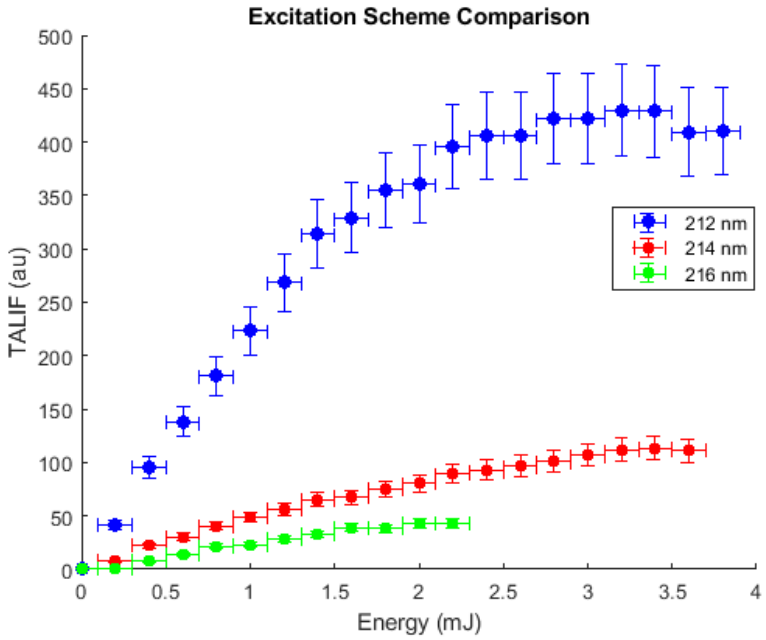

Figure 22. TALIF Energy Schemes Signal Strength Comparison.

Overall, the data in presented in this thesis appendix is collected using the 212.6 nm excitation scheme. The laser energy was set to ~2.0 mJ, as that energy maximizes the signal response while also considering factors such as dye lifetime.

A.3 Results

A.3.1 Cold Flow Results

The study author conducted a series of cold flow measurements (with the cathode turned off) to characterize the cathode flow and diagnostic system before taking measurements with the operating cathode. Figure 23 displays radial profiles at a position 1 cm below the cathode for flow rates of 0, 5, 10, and 15 SCCM. Each profile peaks near $r = 0$, with some minor discrepancies due to zeroing errors in our stage system, and shows a relatively symmetric decay at higher radial values. The peak value (at $r = 0$) of each profile increases approximately linearly with chamber pressure, which rises roughly in proportion to flow rate due to our limited pumping speed. This linear relationship between pressure and flow rate aligns with our lab's previous findings [47,48].

The author selected a flow rate of 7.5 SCCM for our spatial-mapping study because it scales well with peak anode power supply operating currents of 13 A. This flow rate is comparable to conditions used for Hall thrusters in electric propulsion environments at CSU, while also ensuring a sufficient signal-to-noise ratio [48]. In this study, the author used both 5 A and 13 A currents: 5 A corresponds to a propellant-rich regime, and 13 A to a propellant-lean regime, both relevant to the electric propulsion community.

In the radial plots in Figure 23 for both cold flow and plasma (discussed in the next subsection), error bars on the radial axis account for the radial translation stage movement error of approximately 2 mm, which is consistently applied throughout this paper. TALIF signal error bars are based on fluctuations in the dye laser and peak frequency tuning. For these plots, y-direction error bars are included to represent TALIF signal variations: 15% for $z > 1$ cm and 20% closer to the HC orifice, due to the sensitivity of flow, plasma ionization, and luminosity in that region.

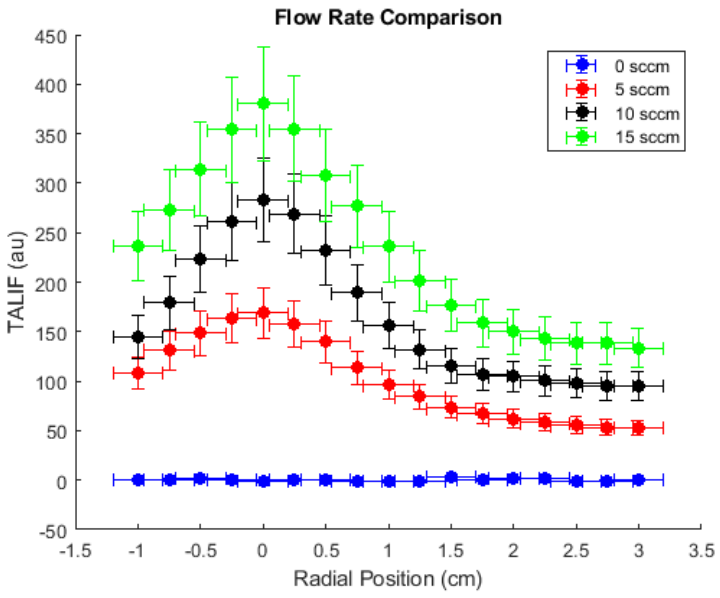

Figure 23. Comparison of Cold Flow Rate and Resulting TALIF Signal Strength for Radial Scans

To begin the mapping of 2D krypton spatial profiles, we validated the spatial mapping of krypton, using experimental cold gas flow data. Figure 24 shows the results of 2D TALIF krypton neutral density mapping. The data trends with what is expected from overall flow behavior, in that greater krypton density is seen nearest the cathode orifice.

Here there is a slight error in that the peak appears to be slightly to the right of the r = 0 location, but this is likely an artifact of translation stage error on order of ~1 mm, and possible slight misalignment of the cathode within the keeper, causing a slight deflection of the cold krypton flow.

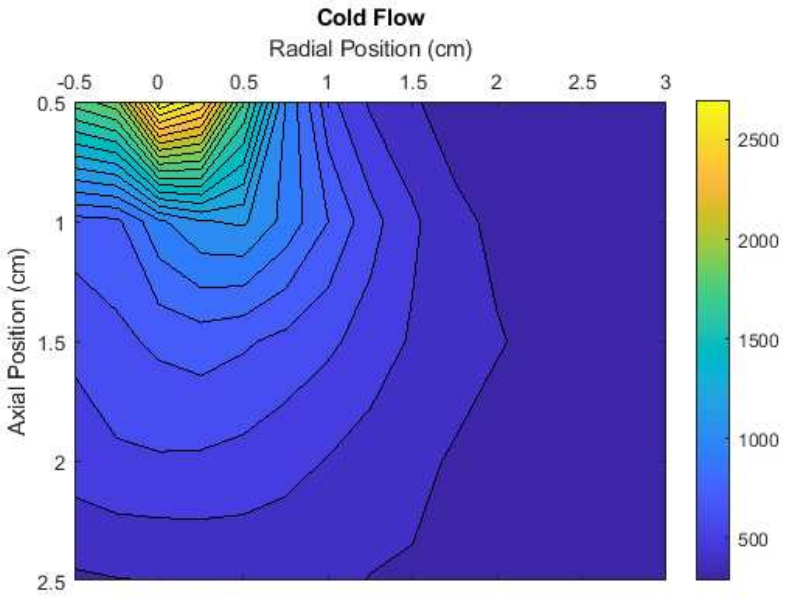

Figure 24. Cold Flow Spatial Map, from z = 0.5 cm below HC to z = 2.5 cm below, oriented with HC keeper orifice oriented above the r = 0 position. Radial data collected from r = -0.5 cm (left of HC) to r = 3.0 cm (right of HC).

A.3.2 Plasma Results

In this subsection, TALIF results for spatially resolved krypton density profiles from operating the cathode are displayed. The cathode was operated with the anode at either

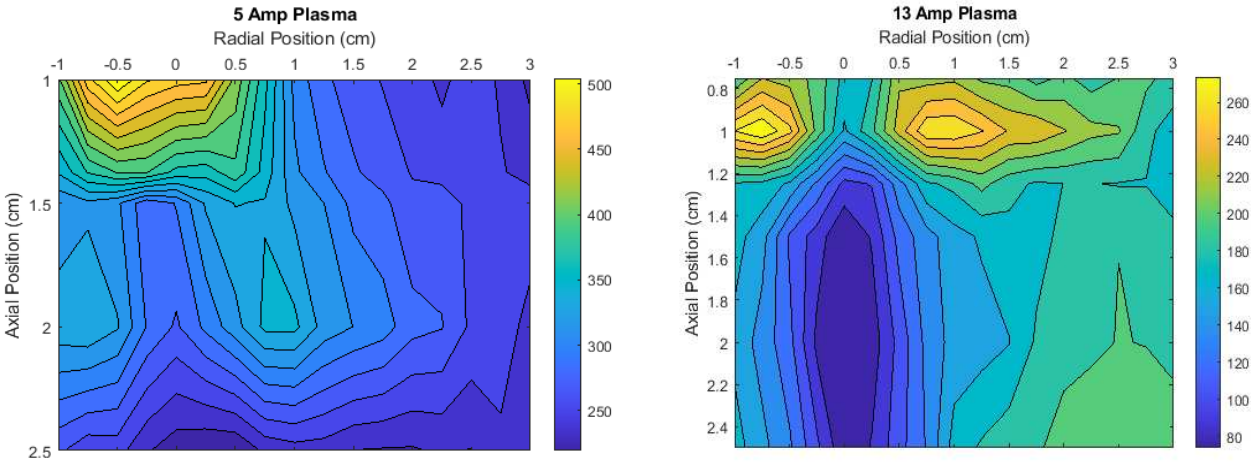

Figure 25. On left, plasma flow at 5 A, with downward dimensions from z = 1.0 cm below HC to z = 2.5 cm below. Color mapping represents the TALIF signal (au). Radial data collected from r = -1.0 cm (left of HC) to r = 3.0 cm (right of HC). On right, plasma flow at 13 A, from 0.75 cm below HC to 2.5 cm below. Radial data collected from 1.0 cm left of HC to 3.0 cm right of HC.

5 or 13 A and a krypton flow rate of 7.5 SCCM. Note that spatial maps for both conditions are shown in Figure 25, with additional 2D ("x-y") plots provided in the appendix (Figures 26-28).

Figure 25 above indicates that in the 5 A regime, the plasma begins to create a neutral density depletion region beneath the keeper orifice. Although the peak neutral density is observed under the orifice, it starts to dip at the r = 0 position. From z = 1.5 cm to z = 2.5 cm, a depletion region forms, with higher neutral density nodes on either side. This trend is more pronounced in the 13 A plasma condition, where two high-density nodes are visible beside the keeper orifice, and a low-density channel develops directly below the r = 0 radial position.

This depletion region may be due to a decrease in neutral density caused by thermal gas expansion [25,43,47,48,52]. However, increased ionization within the plasma plume and a transition from "spot" mode to "plume" mode could also contribute to the observed depletion regions. Modeling work by the Jet Propulsion Laboratory has demonstrated neutral depletion downstream of a LaB6 HC in a propellant-lean regime [26,53]. It is important to note that not all

studies report these depletion areas. For instance, a study of the NEXIS HC did not show depletion zones in propellant-lean mode [54]. This discrepancy might be due to the use of an older version of the 2-D axisymmetric Orificed Cathode (OrCa2D) model in that study, while later studies from JPL that observed the depletion used an updated OrCa2D model.

The updates to the OrCa2D model include enhanced characterization of the transition from low-Knudsen-number incompressible flow within the cathode to compressible, high-Knudsen-number flow in the orifice and downstream plume [26]. These improvements allow for more accurate modeling of neutral behavior. Additionally, the newer versions of the model incorporate ionization and charge-exchange processes, accounting for both source and drag effects [26]. Consequently, it is possible that these neutral depletion regions were not fully characterized in the NEXIS study. Although determining whether a plasma is in "spot" or "plume" mode can be straightforward by measuring the keeper voltage for fluctuations [55], the author was unable to verify these fluctuations due to the cathode being near the end of its operational life.

A.4 Discussion and Extra Figures

In this study, the author utilized TALIF to measure and record spatial profiles (maps) of krypton (Kr) density. By evaluating three different wavelength excitation schemes, it was possible to assess their signal strengths and laser energy dependencies, finding results consistent with previous research. The research has generated spatially resolved maps of krypton flow for both cold flow and plasma conditions, depending on cathode current. The cold flow spatial map shows results that match expected behavior of gas flow through an orifice.

Under propellant-lean operating conditions, the author observed low-density regions of krypton neutrals downstream of the BaO HC, particularly along the orifice centerline. These low-

density regions may be associated with transitions between spot and plume modes, potentially influenced by increased ionization or gas expansion due to plasma heating. These findings are relevant for the electric propulsion community, providing insights into the physical behavior and modeling of BaO HCs.

The spatial data presented here indicate neutral depletion in the plasma plume of a BaO HC and will contribute to numerical modeling efforts aimed at characterizing downstream flow fields in HCs.

In the three Figures 26-28 below, the linear plots for the spatial maps are given, allowing a different perspective on the data presented in this study. The transition in the likely spot-to-plume mode is still quite clear during the transition from cold flow to 5 A plasma to 13 A plasma.

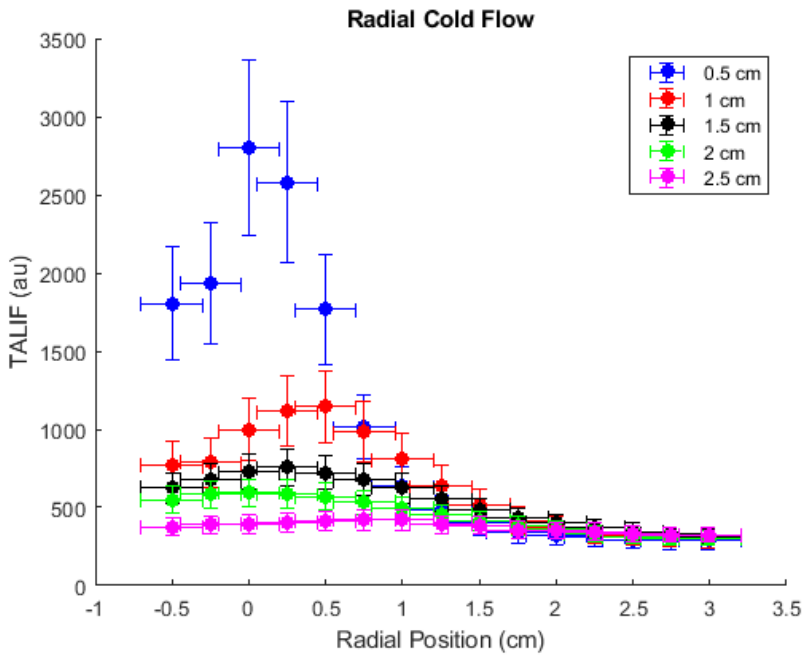

Figure 26. Cold Flow from Fig. 24 in linear format.

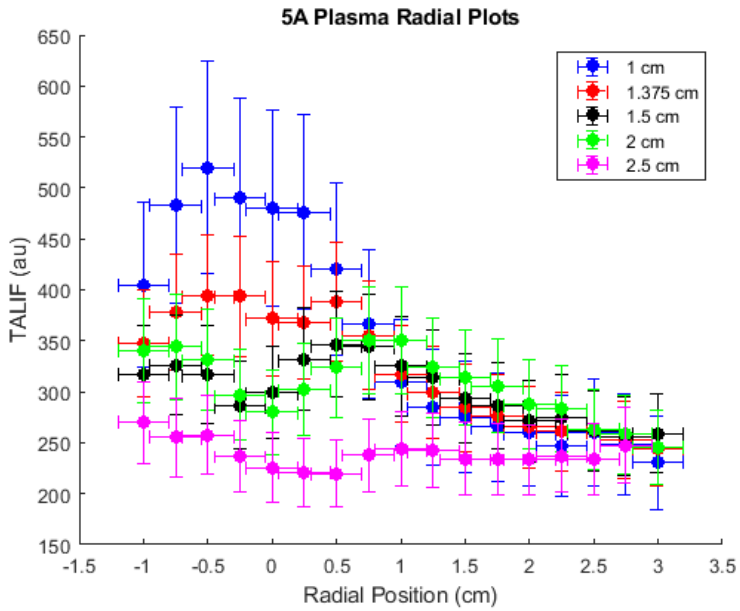

Figure 27. Plasma 5A flow from Fig. 25 in linear format.

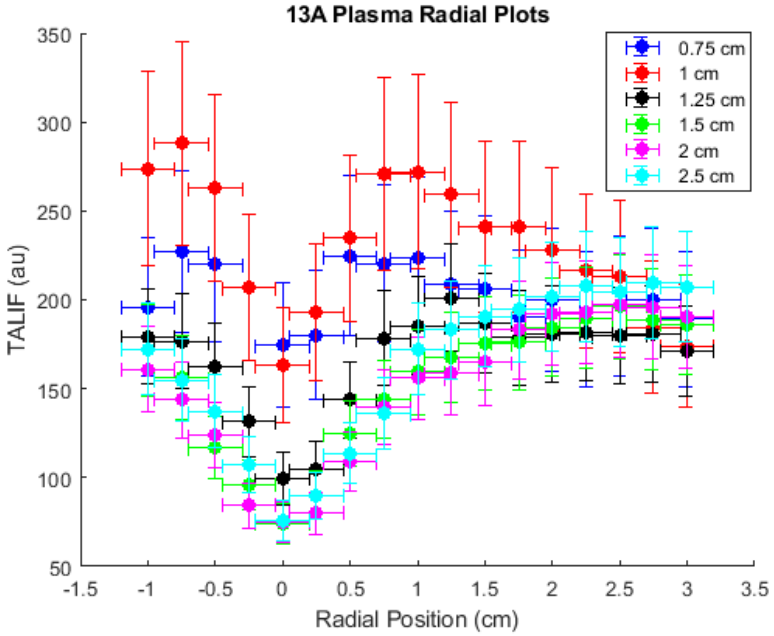

Figure 28. Plasma 13A flow from Fig. 25 in linear format.